NIST Technical Note
NIST TN 2352

Evaluation of Variations in Solution Annealing, Intercritical Annealing, and Aging Treatments on Cobalt-free Maraging Steels

Nicholas Derimow
Jake T. Benzing
Alec I. Saville
Cassidy R. Allen
Jordan Weaver
Nik Hrabe
Timothy P. Quinn
Timothy S. Weeks
Newell Moser
Chad Beamer
Christin Aumayr
Tilman Seifert
Michael Hirtler

This publication is available free of charge from:
https://doi.org/10.6028/NIST.TN.2352

NIST NATIONAL INSTITUTE OF STANDARDS AND TECHNOLOGY
U.S. DEPARTMENT OF COMMERCE

NIST Technical Note
NIST TN 2352

Evaluation of Variations in Solution Annealing, Intercritical Annealing, and Aging Treatments on Cobalt-free Maraging Steels

Nicholas Derimow
Jake T. Benzing
Nik Hrabe
Timothy P. Quinn
Timothy S. Weeks
Newell Moser
Applied Chemicals and Materials Division
Material Measurement Laboratory

Alec I. Saville
Applied Chemicals and Materials Division
Material Measurement Laboratory
Elementum 3D, Colorado, USA

Cassidy R. Allen
Applied Chemicals and Materials Division
Material Measurement Laboratory
College of Engineering and Applied Science
University of Colorado, Boulder, USA

Jordan Weaver
Intelligent Systems Division
Engineering Laboratory

Chad Beamer
Quintus Technologies, Ohio, USA

Christin Aumayr
Tilman Seifert
Michael Hirtler
voestalpine BÖHLER Edelstahl, Austria

This publication is available free of charge from:
https://doi.org/10.6028/NIST.TN.2352

September 2025

U.S. Department of Commerce
Howard Lutnick, Secretary

National Institute of Standards and Technology
Craig S. Burkhardt, Acting NIST Director and Under Secretary of Commerce for Standards and Technology

Certain equipment, instruments, software, or materials, commercial or non-commercial, are identified in this paper in order to specify the experimental procedure adequately. Such identification does not imply recommendation or endorsement of any product or service by NIST, nor does it imply that the materials or equipment identified are necessarily the best available for the purpose.

Publication History
Approved by the NIST Editorial Review Board on 2025-09-17

How to cite this NIST Technical Series Publication:
Derimow, N., Benzing, J. T., Saville, A. I., Allen, C. R., Weaver, J., Hrabe, N., Quinn, Timothy P., Weeks, Timothy, S., Moser, N., Beamer, C., Aumayr, C., Seifert, T., Hirtler, M. (2025) Evaluation of Variations in Solution Annealing, Intercritical Annealing, and Aging Treatments on Cobalt-free Maraging Steels. (National Institute of Standards and Technology, Gaithersburg, MD), NIST TN 2352. https://doi.org/10.6028/NIST.TN.2352

Author ORCID iDs
Nicholas Derimow: 0000-0001-7526-1836
Jake T. Benzing: 0000-0002-7266-870X
Alec I. Saville: 0000-0001-9245-7056
Jordan Weaver: 0000-0003-4857-5164
Nik Hrabe: 0000-0001-7585-0980
Timothy S. Weeks: 0000-0001-8553-2505
Newell Moser: 0000-0002-3346-6427

Contact Information
nicholas.derimow@nist.gov

Submit Comments
nicholas.derimow@nist.gov
325 Broadway
Mail Stop 647
Boulder, Colorado 80305

Abstract

This work is a compilation and summary of the quasi-static mechanical properties of a novel cobalt-free maraging steel, M789, that underwent a series of heat treatments which included solution annealing, intercritical annealing, and aging. This work utilized a single laser powder bed fusion (PBF-L) build to ensure uniform chemistry of the batch of specimens. The tensile geometry consisted of miniaturized tensile specimens, tested to failure to assess properties such as the elastic modulus, yield strength, ultimate tensile strength, uniform elongation, and and total elongation. The results are presented in tabular and graphical format.

Keywords

Additive Manufacturing; Cobalt-free Maraging Steels; Heat Treatments; Laser Powder Bed Fusion; Tensile Properties.

Table of Contents

List of Tables

List of Figures

1. Introduction

There has been growing interest in the research and development of industrially relevant materials [1] that do not rely on critical minerals [2]. One such class of materials is *maraging* steels (where *maraging* is a combination of the words *martensitic* and *aging*). While there exists classes of steels that predominantly consist of martensitic phases, maraging steels are distinct in that the aging process produces intermetallic precipitate phases that strengthen the steel [3–7]. Maraging steels are often desirable in applications that require high strength and toughness, such as the aerospace and manufacturing tooling industries [8, 9]. Aside from iron (Fe), one of the principal alloying components in maraging steels is cobalt (Co), an elemental metal refined from a critical mineral. While cobalt-free maraging steels have been studied since the 1990s [5, 10], recent interest in these alloys has been reinvigorated by the geometrical design freedom of additive manufacturing (AM), such as laser powder bed fusion (PBF-L).

A recent review by Narasimharaju et al. covers AM studies of various steels manufactured by PBF-L, where typically the goal is to reach, or even surpass, the mechanical properties of their wrought counterparts [11]. Another recent review focuses specifically on the AM studies of 18% (wt.%) Ni-containing maraging steels, such as M200, M250, M300, and M350–all of which, however, contain Co in percentages ranging from 8 wt.% to 12.5 wt.%. Of the 18% Ni maraging steels, M300 produced via PBF-L has been of particular interest [12], with studies that have investigated the as-built properties [13], tensile properties [14, 15], effects of build parameters [15–18], surface finish and fatigue [19, 20], effects of heat and post-processing treatments [21, 22], and magnetic properties [23].

Deviating from the 18% Ni-containing maraging steels, the development of a maraging steel by voestalpine BÖHLER Edelstahl, designated as *M789* [24] in 2019, contains the nominal chemistry presented in Table 1 where one of the defining characteristics is that Cr is substituted in chemical concentration in place of Co. The recent development of M789 has spawned several theses [25–31], as well as studies that have investigated the PBF-L of M789 with respect to hybrid processes [32, 33], microstructure [34–36], mechanical properties [35, 37, 38], fatigue properties [19, 39], corrosion behavior [39], as well as the effect of varying build parameters [40, 41]. There have also been several studies that have leveraged directed energy deposition (DED) AM to study M789 [42, 43].

Work on the heat treatment optimization of PBF-L M789 has resulted in ultimate tensile strengths that are approximately 1.8 GPa [35, 37, 44] when solution annealing was carried out at 1000 °C for 1 h, followed by aging at 500 °C for up to 2 h - 9 h to precipitate the strengthening intermetallic $Ni_3(Ti,Al)$ (η) phase. A study that skipped the solution annealing step and have opted for *direct aging* from the PBF-L as-built condition at 500 °C resulted in strengths of up to 1.6 GPa [38].

Based on the aforementioned work, as well as communication with the M789 feedstock manufacturer, the heat treatment parameters that have produced the most consistently

high strengths have been solution annealing at 1000 °C for 1 h and aging at 500 °C for 3 hours. For the purpose of the present investigation, this heat treatment will be referred to as the *baseline* heat treatment condition. The aim of this study is to iterate upon the baseline heat treatment to interrogate the heat treatment parameters for potential avenues to increase the mechanical properties of M789. This is a continuation of the work presented in Ref. [41], where the PBF-L process parameters were varied to study the stability of the as-built microstructure.

2. Methods

2.1. Chemistry and Powder Feedstock

The powder feedstock and as-built compositions are included in Table 1 from inductively-coupled plasma mass spectrometry (ICPMS) measurements. Phosphorous and sulfur content were less than 0.005 wt.% and 0.001 wt.%, respectively. The M789 powder consisted of a nominal particle size distribution of 15 μm to 45 μm in diameter, with a D90 of 45 μm.

Table 1. Nominal and chemical composition in weight % as determined by ICPMS for M789 used in this study. Note: trace elements were not measured.

–	C	Al	Si	Ti	Cr	Ni	Mo	Fe
Nominal	$<$0.02	0.60	–	1.00	12.20	10.00	1.00	bal.
Powder	0.013	0.55	0.42	1.00	12.28	10.06	1.00	75.68
As-built	0.010	0.52	0.32	0.97	12.31	10.23	0.94	75.64

2.2. Build Parameters

This work builds off of a previous study carried out at NIST by Saville et al. [41], where the PBF-L parameter set was varied in order to study the microstructure and mechanical properties of the as-built condition. In the present work, we adopt the same nomenclature used in Ref. [41], and investigate iterations of heat treatments using build parameter set *A*, which consisted of PBF-L on an EOS M290 machine (software: EOSPRINT 1.9) with a laser power of 370 W, velocity of 800 mm/s, hatch spacing of 100 μm, scan rotation of 67°, and volumetric energy density of 81 J/mm^3.

The PBF-L build utilized a 1045 steel build plate, 80 °C build plate heating, 60 μm layer thickness, a ceramic recoating blade, grid nozzle, and an argon gas environment. Build specimens consisted of cubes measuring 20 mm $\times$ 20 mm $\times$ 20 mm, which were removed from the build plate by wire electrical discharge machining (wire-EDM). An image of the build plate can be seen in Fig. 1.

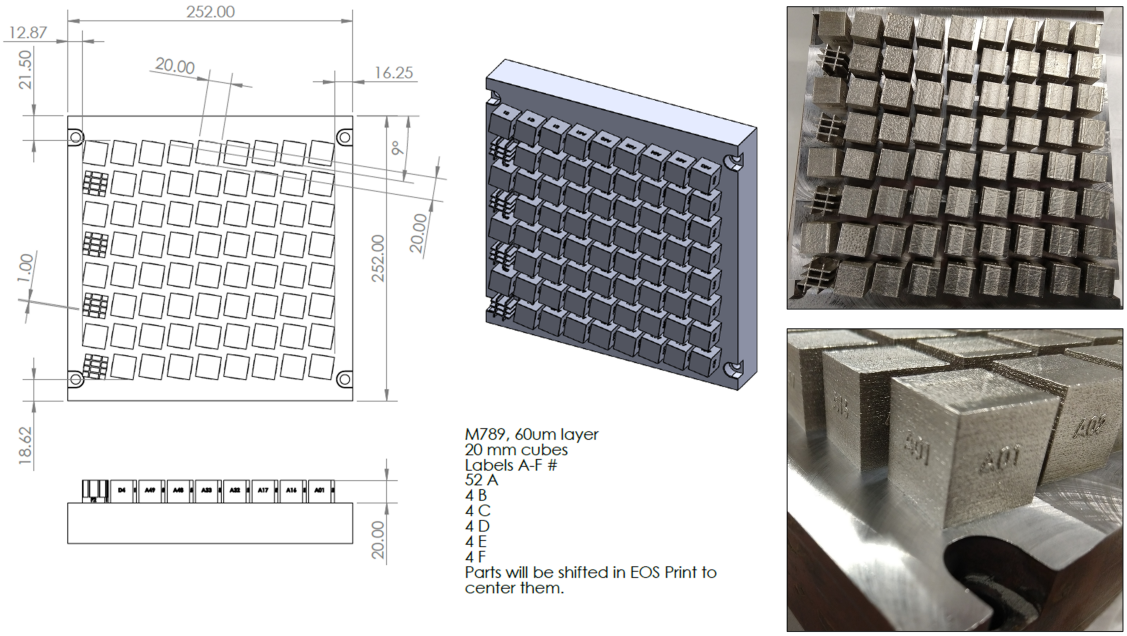

Fig. 1. Schematic of the build plate and pictures of the 20 mm cubes. Note, labels B–F pertain to a different study.

2.3. Heat Treatments

The aim of this work was to iterate upon the baseline heat treatment condition, shown in Table 2. Condition A1 pertains to the as-built condition, whereas condition A3 was cryogenically treated at 8 mK for approximately 600 hours, and condition A4 at 2.3 K for approximately 18 hours–all of which were omitted from Table 2 for brevity. The numbering of the specimens are consistent with previous work [41], however, were down-selected such that there are specimens omitted from this work, for example *A2*. The heat treatment schema was from left to right and air cooled in between steps, unless otherwise indicated. A pictorial flow chart, shown in Fig. 2, depicts the temperatures used in this study, however without times. An *intercritical* annealing step was investigated at several temperatures between first heat treatment (annealing) step of 1000 °C and aging step 500 °C to elucidate the potential for metastable austenite formation, which could contribute to different types of precipitates during the aging treatments and/or lead to martensite formation/hardening during plastic deformation. The aging temperatures were also varied between 475 °C, 500 °C, and 510 °C to investigate the potential for new precipitates to form.

The A32 and A34 specimens that underwent hot isostatic pressing (HIP) treatments at 500 °C and 1000 °C followed by 500 °C at 200 MPa of Ar, respectively, and were air cooled.

Table 2. Heat treatment conditions used in this study, where the matrix elements are expressed in time (h) for each temperature (°C). The heat treatment schema was from left to right, unless otherwise indicated (such as in A14). WQ = water quench, S = series solution treatment (no removal from furnace), HIP = hot isostatic pressure treatment.

Condition	1000 °C	825 °C	775 °C	750 °C	510 °C	500 °C	475 °C
A5	1 h	–	–	–	–	–	–
A6	1 h (WQ)	–	–	–	–	–	–
A7	1 h	–	–	–	–	3 h	–
A8	–	–	–	–	–	3 h	–
A9	–	–	1.5 h	–	–	–	–
A10	–	–	1.5	–	–	3 h	–
A11	1 h	–	–	–	–	–	3 h
A12	1 h	–	–	–	3 h	–	–
A13	1 h	–	1.5 h	–	–	3 h	–
A14	1 h	–	–	–	1.5 h (2nd)	–	1.5 h (1st)
A15	–	–	–	–	–	–	3 h
A17	–	–	–	1.5 h	–	–	–
A18	–	1.5 h	–	–	–	–	–
A20	1 h (S)	–	1.5 h (S)	–	–	–	–
A21	1 h (S)	–	1.5 h (S)	–	–	3 h (S)	–
A22	1 h (S)	–	–	–	–	3 h (S)	–
A23	–	–	1.5 h (S)	–	–	3 h (S)	–
A32	–	–	–	–	–	3 h (HIP)	–
A34	1 h (HIP)	–	–	–	–	3 h (HIP)	–
A41	1 h	–	8 h	–	–	–	–
A42	1 h	–	8 h	–	–	3 h	–

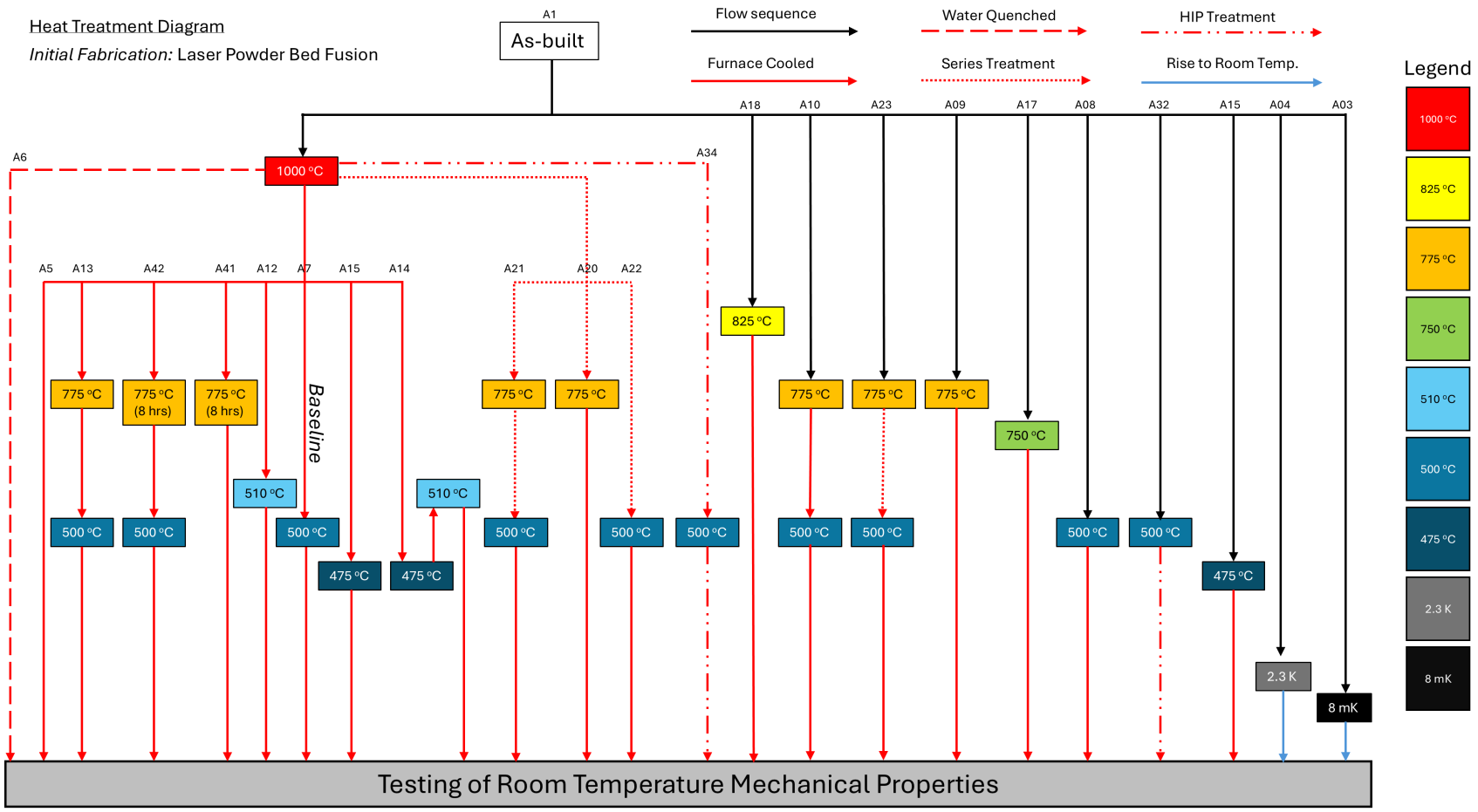

Fig. 2. Heat treatment flowchart.

2.4. Mechanical Testing

Tensile properties of as-built microstructures were measured using an extensometer instrumented load frame using a quasi-static strain rate of 10^{-3} s^{-1} and a custom tensile geometry based closely on ASTM E8 [45], inspired by recent work on the repeatability of tests on sub-standard sized miniature tensile specimens [46]. The design is depicted in Fig. 3, with a nominal gauge length of 5.5 mm, width of 1.25 mm, and thickness of 1 mm.

An image of the load frame used in this study is shown in Fig. 4a. Strain was measured using an extensometer with maximum gauge length of 3 mm (Fig. 4b). Due to the design gauge length being 5.5 mm, any specimens that failed outside of the extensometer gauge measurement length of 3 mm or on the extensometer pins were excluded from analysis that required the total elongation. That is, these tests were not used to measure total elongation.

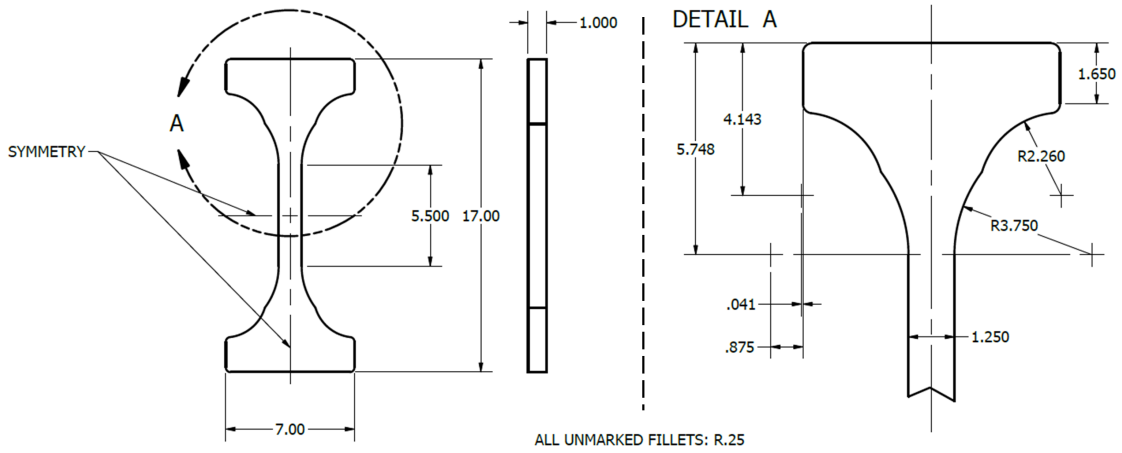

Fig. 3. Tensile geometry used in this study.

2.5. Uncertainty Analysis

The calculation of the stress uncertainty as part of the tensile testing for a rectangular cross sectional area can be defined in units of F and δF for force (N), and t and δt and w and δw for thickness and width (mm), respectively. Therefore, the stress, σ is represented by:

$$\sigma = \frac{F}{t \cdot w} \tag{1}$$

and uncertainty for a rectangular cross section via the root-sum-squares method [47]:

$$\delta\sigma = \sqrt{\delta w^2 \left(\frac{F}{t \cdot w^2}\right)^2 + \delta t^2 \left(\frac{F}{t^2 \cdot w}\right)^2 + \delta F^2 \left(\frac{1}{t \cdot w}\right)^2} \tag{2}$$

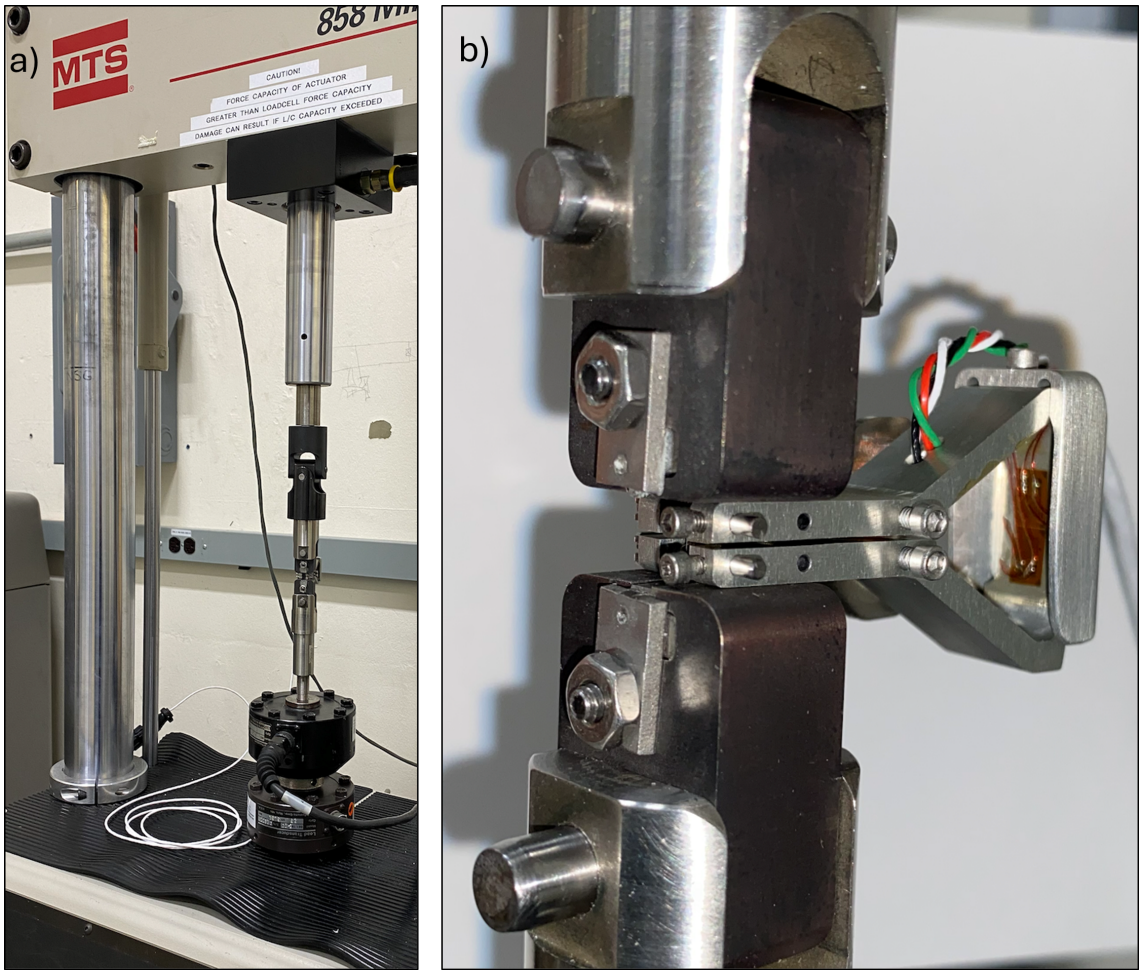

Fig. 4. a) Image of the load frame used in this work and b) image of the extensometer.

The calibration uncertainty in the load cell was last measured to be 0.27%, therefore, this value is applied to the average yield and ultimate tensile stress values for the uncertainty measurement in stress, whereas 0.01 mm was used for the uncertainty in the cross sectional area as measured via digital caliper prior to each test.

3. Results

The average mechanical properties for the heat treatment iterations are presented in Table 3, whereas bar charts that visually compare the conditions are presented in Fig. 5 for yield strength (σ_{YS}), Fig. 6 for ultimate tensile strength (σ_{UTS}), Fig. 7 for elastic modulus (E), Fig. 8 for uniform elongation (ε_u), and Fig. 9 for total elongation (ε_t). It is notable that the total elongation (ε_t) averages have been filtered such that only tests that reached failure inside the pins of the extensometer are reported, represented by ε_t(N) in Table 3. The color schemes for the bar charts incorporate the colors of the temperatures utilized for each

heat treatment, and the gradient color schemes represent continuous heat treatments such that the specimens never left the furnace. The standard deviations represent the standard error of the mean for each data set. The engineering stress-strain curves for each of the conditions are presented in Appendix A. The true stress-strain curves are presented in Appendix B.

Table 3. Summary of mechanical properties for each heat treatment condition. The total elongation data has been filtered such the averages are only representative of tests that reached failure within the measurement portion of the physical extensometer. σ_{YS} = yield strength, σ_{UTS} = ultimate tensile strength, E = elastic modulus, ε_u = uniform elongation, and ε_t = total elongation. The $\pm$ values are one standard error of the mean. The total elongation values are accompanied by the number, N, of values used to calculate the standard deviation of the mean.

Condition	σ_{YS} (GPa)	σ_{UTS} (GPa)	E (GPa)	ε_u	ε_t	ε_t(N)
A1	0.75 ± 0.03	1.04 ± 0.01	152 ± 17	0.057 ± 0.005	0.259 ± 0.039	2
A3	0.81 ± 0.02	1.06 ± 0.01	158 ± 8	0.046 ± 0.004	0.275 ± 0.033	2
A4	0.81 ± 0.02	1.05 ± 0.01	152 ± 8	0.048 ± 0.003	0.225 ± 0.063	2
A5	0.74 ± 0.04	0.95 ± 0.02	141 ± 17	0.029 ± 0.003	0.263 ± 0.015	3
A6	0.73 ± 0.04	0.95 ± 0.02	153 ± 29	0.027 ± 0.002	0.280 ± 0.031	5
A7	1.67 ± 0.02	1.75 ± 0.02	173 ± 5	0.020 ± 0.001	0.108 ± 0.055	4
A8	1.41 ± 0.03	1.55 ± 0.05	179 ± 13	0.029 ± 0.013	0.119 ± 0.082	7
A9	0.70 ± 0.02	0.97 ± 0.01	145 ± 15	0.042 ± 0.008	0.249 ± 0.068	3
A10	1.31 ± 0.04	1.45 ± 0.04	174 ± 7	0.054 ± 0.020	0.130 ± 0.060	8
A11	1.62 ± 0.03	1.73 ± 0.03	177 ± 6	0.024 ± 0.002	0.116 ± 0.029	4
A12	1.64 ± 0.01	1.72 ± 0.00	177 ± 4	0.021 ± 0.002	0.119 ± 0.031	9
A13	1.44 ± 0.04	1.54 ± 0.05	181 ± 7.2	0.021 ± 0.002	0.111 ± 0.035	7
A14	1.63 ± 0.01	1.72 ± 0.01	178 ± 5.5	0.022 ± 0.002	0.130 ± 0.041	7
A15	1.43 ± 0.03	1.58 ± 0.01	171 ± 13.9	0.060 ± 0.009	0.211 ± 0.052	8
A17	0.70 ± 0.02	0.98 ± 0.01	145 ± 22.9	0.053 ± 0.004	0.270 ± 0.022	6
A18	0.72 ± 0.03	0.99 ± 0.01	157 ± 20.3	0.037 ± 0.003	0.255 ± 0.019	5
A20	0.75 ± 0.04	0.94 ± 0.01	134 ± 26.0	0.029 ± 0.003	0.266	1
A21	0.75 ± 0.05	0.96 ± 0.01	137 ± 36.5	0.031 ± 0.003	0.257	1
A22	0.73 ± 0.04	0.96 ± 0.01	146 ± 24.8	0.031 ± 0.002	0.206 ± 0.043	3
A23	0.70 ± 0.03	0.99 ± 0.01	146 ± 20.6	0.051 ± 0.003	–	0
A32	1.47 ± 0.05	1.59 ± 0.01	166 ± 17.6	0.024 ± 0.006	0.171 ± 0.067	7
A34	1.65 ± 0.02	1.75 ± 0.01	180 ± 7.0	0.023 ± 0.001	0.144 ± 0.020	7
A41	0.68 ± 0.02	0.97 ± 0.00	145 ± 16.1	0.046 ± 0.003	0.140	1
A42	1.40 ± 0.02	1.49 ± 0.01	181 ± 11.7	0.021 ± 0.002	0.167 ± 0.031	8

The uncertainty in the stress measurement was calculated as a function of the calibration uncertainty of 0.27% for the load cell used in this work, and was plotted against the ultimate tensile strength such that the fractional uncertainty is representative of the indi-

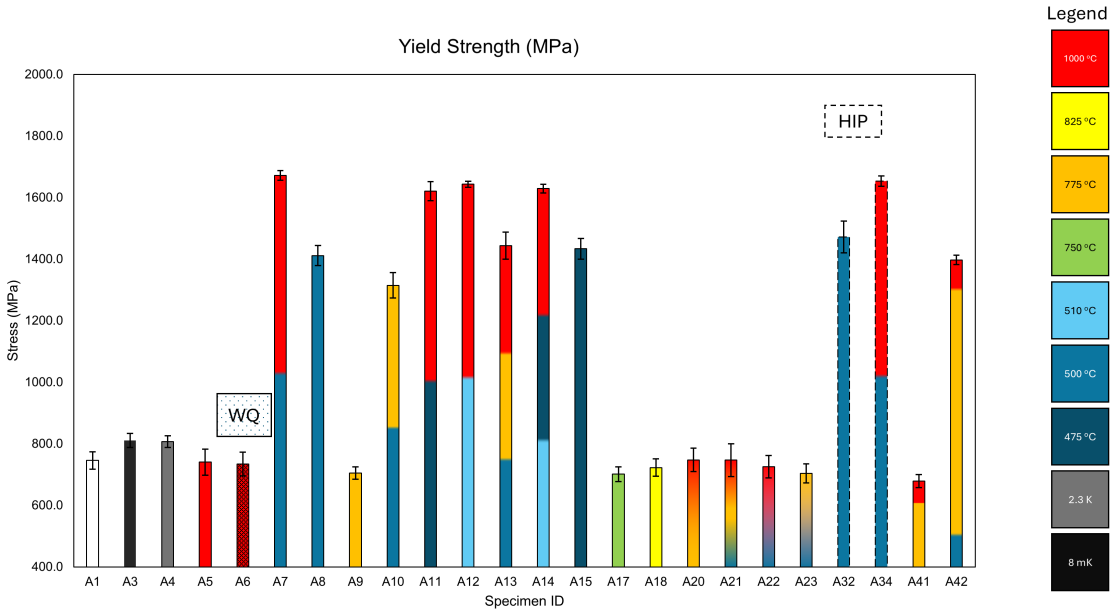

Fig. 5. Summary of the yield strengths measured in this study. Error bars represent one standard deviation of the mean.

vidual value. A scatter plot of all of the fractional uncertainties plotted against the ultimate tensile strengths measured in this work is presented in Fig. 10.

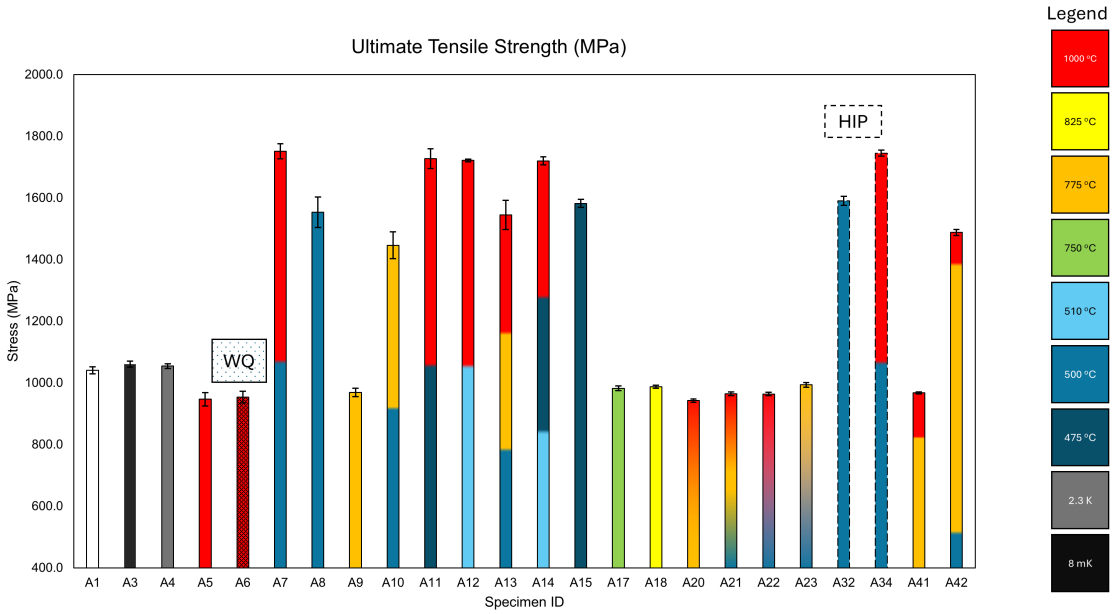

Fig. 6. Summary of the ultimate tensile strengths measured in this study. Error bars represent one standard deviation of the mean.

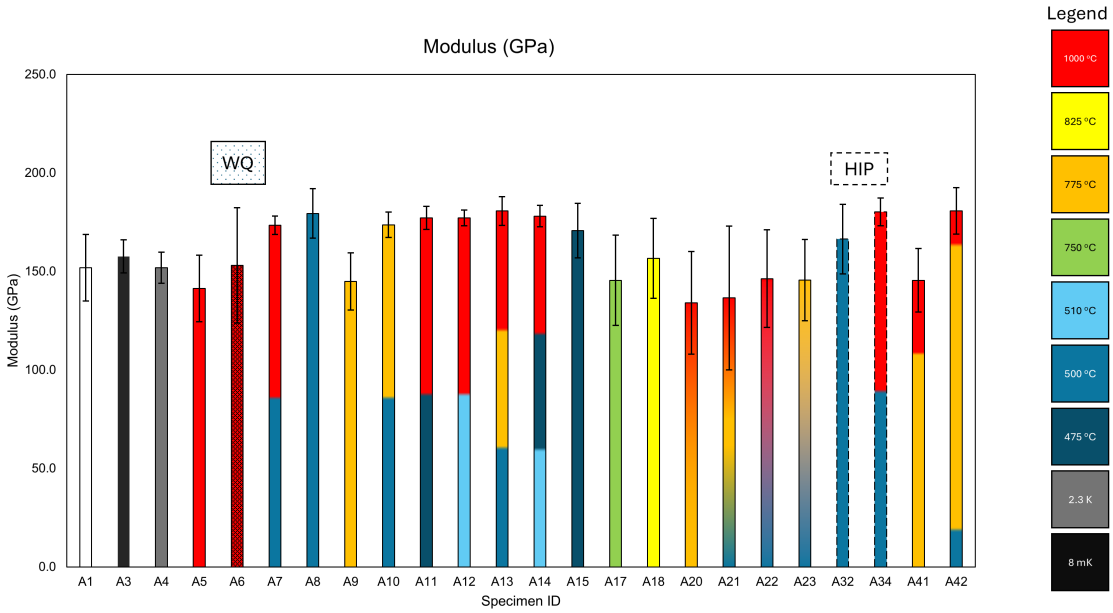

Fig. 7. Summary of the elastic modulus values measured in this study. Error bars represent one standard deviation of the mean.

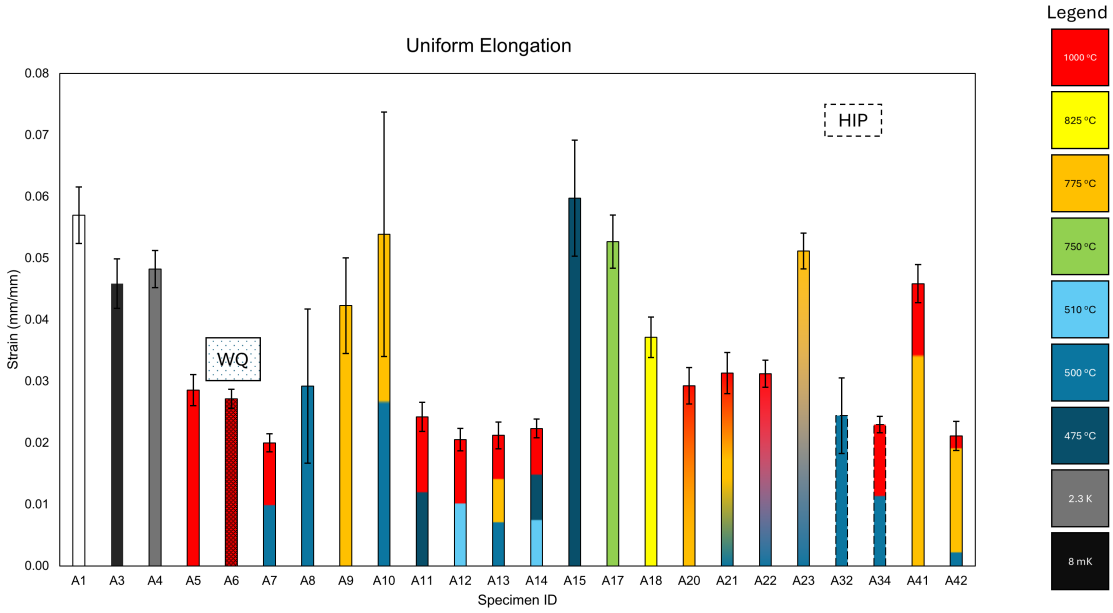

Fig. 8. Summary of uniform elongation values measured in this study. Error bars represent one standard deviation of the mean.

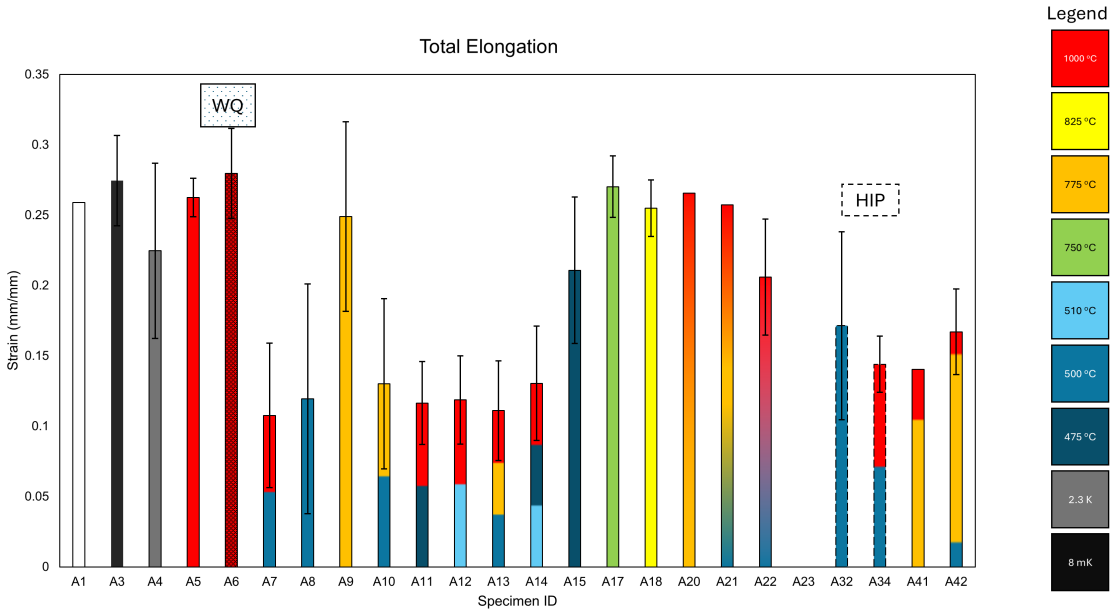

Fig. 9. Summary of the total elongation values measured in this study. Note, the data has been filtered to exclude data tests that exhibited failure outside of the measurement pins of the physical extensometer. Error bars represent one standard deviation of the mean.

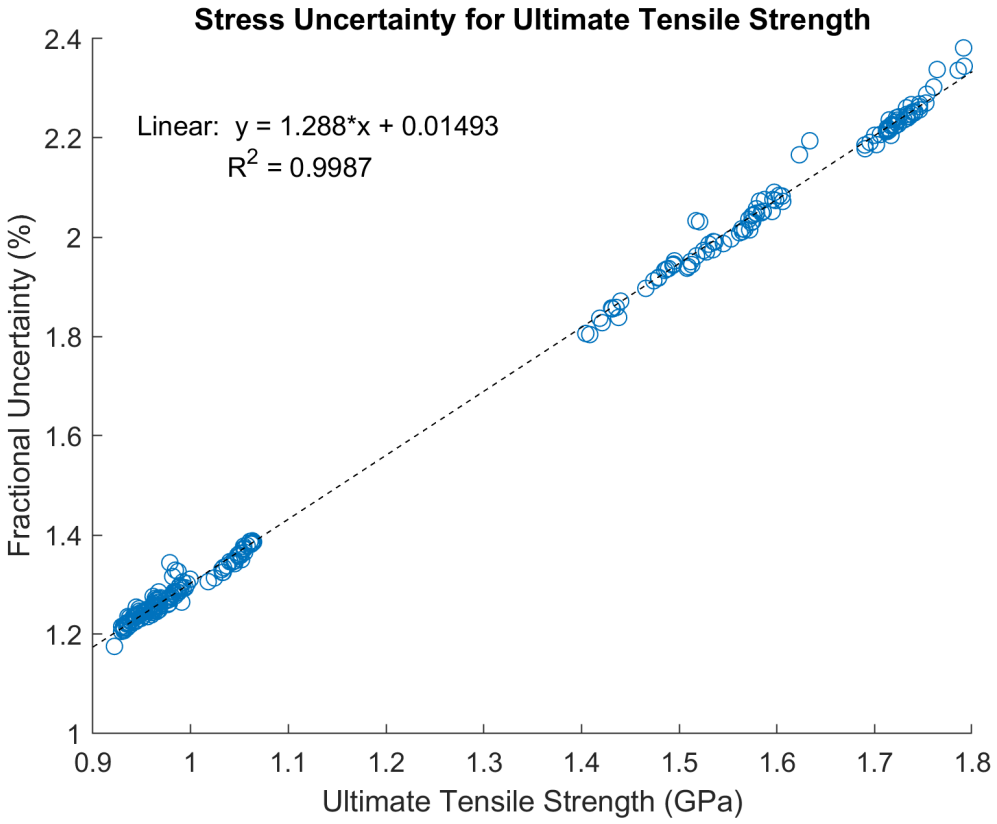

Fig. 10. Fractional uncertainty of the stress measurement plotted against the ultimate tensile strengths measured in this work for all of the test specimens.

4. Summary

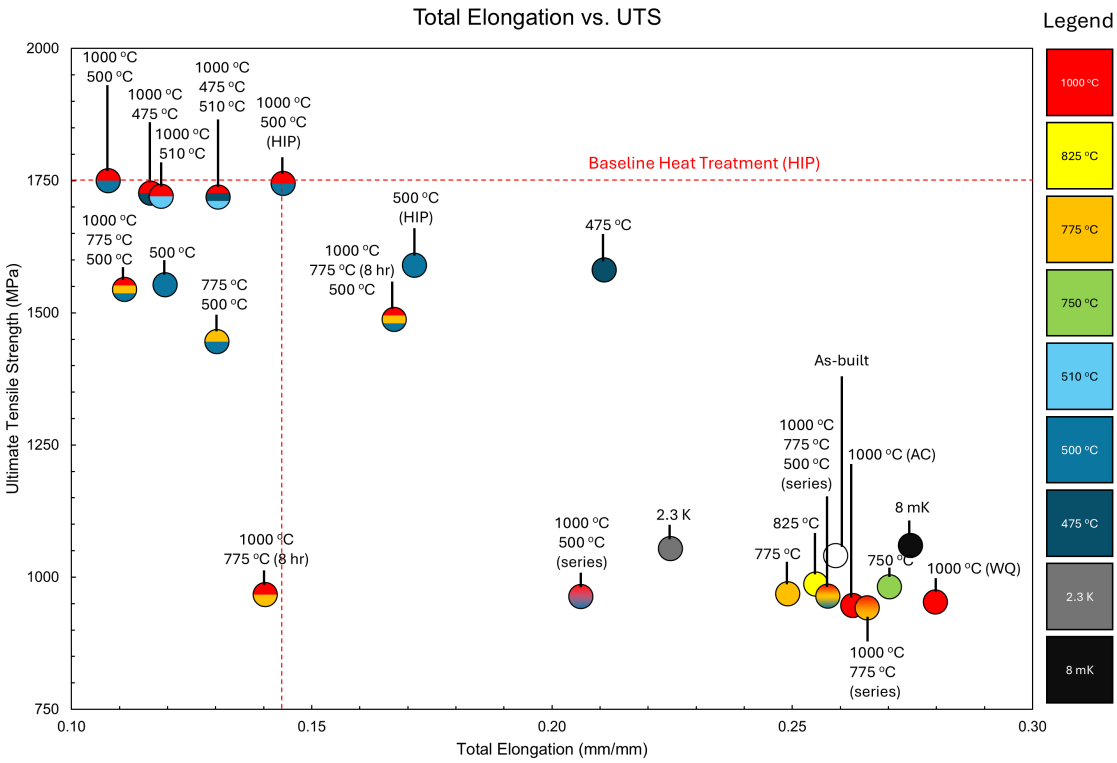

Fig. 11. Summary of ultimate tensile strengths compared to total elongation. The red dashed lines intersect the ultimate tensile strength of the baseline heat treatment condition that was processed via HIP.

A summary plot, which incorporates the color scheme for the heat treatments, is shown for ultimate tensile strengths compared against total elongation for each of the conditions in Fig. 11. The highlighted lines in red are for the properties of the HIP condition of the baseline heat treatment, which is shown to have equal strength but greater ductility, consistent with modern understanding of HIP-induced pore closure leading to increased ductility in metals [48].

Below are the summarized observations from this work:

- The ultimate tensile strength of the baseline heat treatment of approximately 1750 MPa is consistent with previously reported values for M789, and with greater ductility when subjected to hot isostatic pressing treatment.
- None of the heat treatment iterations in this work surpassed the baseline heat treatment in terms of ultimate tensile strength.

- The baseline and direct aging conditions that were replicated with hot isostatic pressing treatments maintained the strength of their non HIP'd counterparts, with increased ductility.
- The annealing-only treatments without aging produced lower strengths but greater ductility.
- The series heat treatments (where the specimens were not removed from the furnace, such that each step cooled to the next temperature) resulted in a drastic decrease in strength relative to their individually segmented counterparts. That is, where each step was allowed to cool prior to the next heat treatment step.
- The cryogenic treatments led to a small increase in the yield strength relative to the as-built condition, however, they converged towards similar values for ultimate tensile strength as the as-built condition.
- The direct aging treatments led to slight decreases in strength, but resulted in greater ductility, and therefore a qualitative improvement in quasi-static toughness.
- The intercritical annealing at 775 °C for 8 hours prior to aging led to an increase in ductility with a slight decrease in ultimate tensile strength relative to the intercritical annealing carried out for 1.5 hours.

Future work will investigate a subset of the heat treatment conditions, shown in Fig. 12, where HIP treatments will be applied to increase the ductility of the heat treatment conditions that utilize full-sized ASTM E8 [45] specimens, as well as the effect of different testing environments.

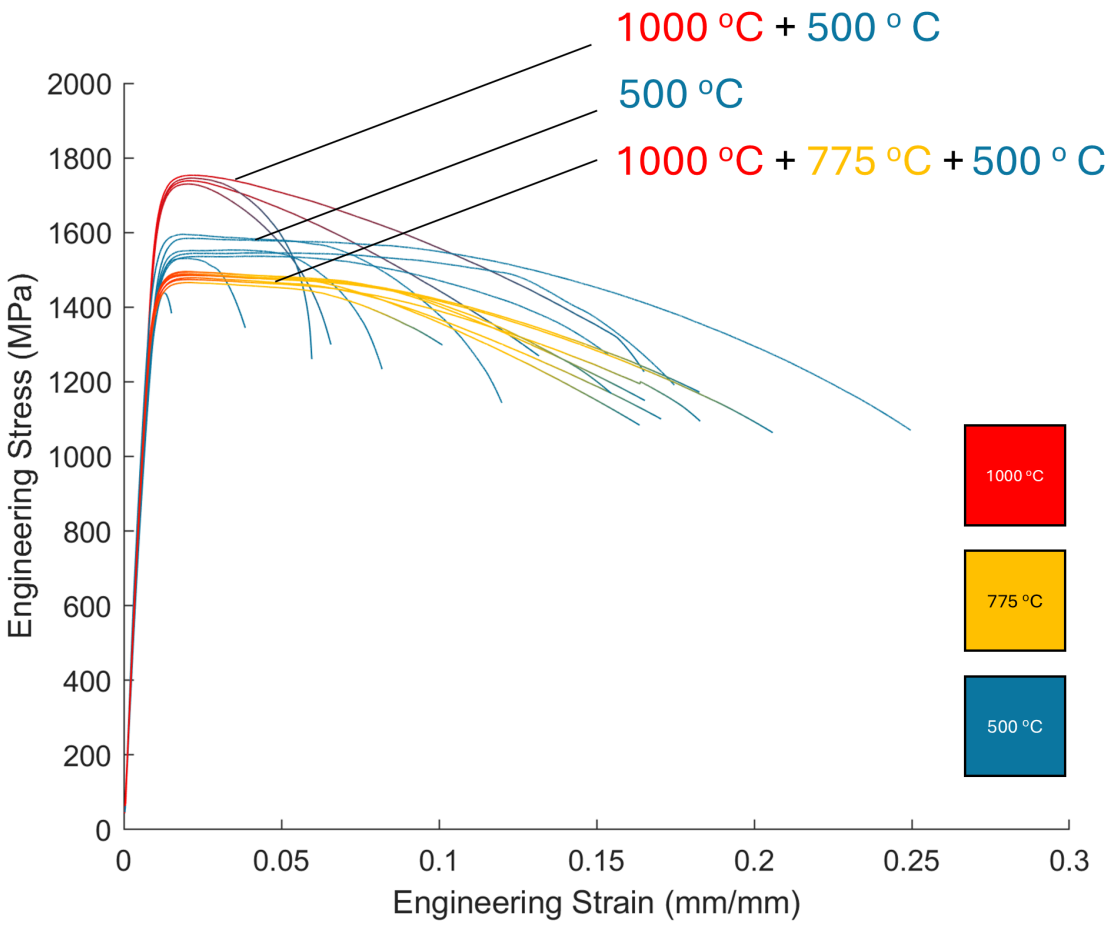

Fig. 12. Engineering stress-strain curves for the baseline, baseline with intercritical annealing (8 hours) and aging, and direct aging conditions. The color gradients for each plot were applied to match the data visualization shown in Fig. 11.

References

[1] Burns C, Livers S, Meher S, Mahmud A, Garcia D, Meher P, Hartmann T, Van Rooyen I, Roy A, Lund B, Nartu MSKKY, Wang T, Fernandez Dos Santos J, Silva C (2024) Development Results on Replacement Materials for Current Scarce or High Supply Chain Risk Materials, . PNNL–36491, 2481601. https://doi.org/10.2172/2481601

[2] Villalobos F, Allendorf E, Caulkins J, Charan S, Yoshiara E, Silberglitt R, Tariq ZH (2024) From Mines to Markets in the Middle East and Central Asia: Critical Mineral Suppliers and Dependencies in the U.S. Central Command Area of Responsibility. *RAND Research Report* (RR-A2914-1). https://doi.org/10.7249/RRA2914-1

[3] Floreen S, Mihalisin JR (1965) *High-Strength Stainless Steel by Deformation at Low Temperatures* (ASTM International100 Barr Harbor Drive, PO Box C700, West Conshohocken, PA 19428-2959), , pp 17–25. https://doi.org/10.1520/STP43726S

[4] Sha W, Cerezo A, Smith GDW (1993) Phase chemistry and precipitation reactions in maraging steels: Part I. Introduction and study of Co-containing C-300 steel. *Metall Trans A* 24(6):1221–1232. https://doi.org/10.1007/BF02668190

[5] Sha W, Cerezo A, Smith GDW (1993) Phase chemistry and precipitation reactions in maraging steels: Part II. Co-free T-300 steel. *Metall Trans A* 24(6):1233–1239. https://doi.org/10.1007/BF02668191

[6] Sha W, Cerezo A, Smith GDW (1993) Phase chemistry and precipitation reactions in maraging steels: Part III. Model alloys. *Metall Trans A* 24(6):1241–1249. https://doi.org/10.1007/BF02668192

[7] Sha W, Cerezo A, Smith GDW (1993) Phase chemistry and precipitation reactions in maraging steels: Part IV. Discussion and conclusions. *Metall Trans A* 24(6):1251–1256. https://doi.org/10.1007/BF02668193

[8] Weiss BZ (1983) Maraging Steels—Structure, Properties and Applications. *Specialty Steels and Hard Materials* (Elsevier), pp 35–54. https://doi.org/10.1016/B978-0-08-029358-5.50009-4

[9] Habiby F, Ul Haq A, Khan A (1994) The Properties and Applications of 18% Nickel Maraging Steels. *Materials Technology* 9(11-12):246–252. https://doi.org/10.1080/10667857.1994.11785084

[10] Gemperle A, Gemperlová J, Sha W, Smith GDW (1992) Aging behaviour of cobalt free chromium containing maraging steels. *Materials Science and Technology* 8(6):546–554. https://doi.org/10.1179/mst.1992.8.6.546

[11] Narasimharaju SR, Zeng W, See TL, Zhu Z, Scott P, Jiang X, Lou S (2022) A comprehensive review on laser powder bed fusion of steels: Processing, microstructure, defects and control methods, mechanical properties, current challenges and future trends. *Journal of Manufacturing Processes* 75:375–414. https://doi.org/10.1016/j.jmapro.2021.12.033

[12] Mooney B, Kourousis K (2020) A Review of Factors Affecting the Mechanical Properties of Maraging Steel 300 Fabricated via Laser Powder Bed Fusion. *Metals* 10(9):1273. https://doi.org/10.3390/met10091273

[13] Zaba K, Balcerzak M, Kuczek Ł, Wiewióra M, Różycka I, Trzepieciński T, Mizera J (2024) Application of Powder-Bed Fusion of Metals Using a Laser for Manufacturing of M300 Maraging Steel Tools Intended for Sheet Metal Bending. *Materials* 17(24):6185. https://doi.org/10.3390/ma17246185

[14] Suryawanshi J, Prashanth K, Ramamurty U (2017) Tensile, fracture, and fatigue crack growth properties of a 3D printed maraging steel through selective laser melting. *Journal of Alloys and Compounds* 725:355–364. https://doi.org/10.1016/j.jallcom.2017.07.177

[15] Vishwakarma J, Chattopadhyay K, Santhi Srinivas N (2020) Effect of build orientation on microstructure and tensile behaviour of selectively laser melted M300 maraging steel. *Materials Science and Engineering: A* 798:140130. https://doi.org/10.1016/j.msea.2020.140130

[16] De Baere D, Moshiri M, Smolej L, Hattel JH (2022) Numerical investigation into laser-based powder bed fusion of cantilevers produced in 300-grade maraging steel. *Additive Manufacturing* 50:102560. https://doi.org/10.1016/j.addma.2021.102560

[17] Omidi N, Farhadipour P, Barka N (2023) Investigation into the effect of the SLM processing parameters on the microstructure and mechanical behavior of M300; experimental and statistical analysis. *Int J Adv Manuf Technol* 129(9-10):4419–4434. https://doi.org/10.1007/s00170-023-12495-7

[18] Petersen HE, Sampson BJ, Failla DP, Priddy MW, McClelland ZB (2023) The Variation of Mechanical Properties of M300 Maraging Steel Manufactured with Varying Process Parameters in Laser Powder Bed Fusion. *Solid Freeform Fabrication 2023: Proceedings of the 34th Annual International Solid Freeform Fabrication Symposium – An Additive Manufacturing Conference* https://doi.org/10.26153/TSW/50977

[19] Ordnung D, Mertens T, Tacq J, Nasab MH, Sinico M, Li G, Thijs L, Vrancken B, Van Hooreweder B (2024) Enhancing fatigue life of as-printed martensitic M789 steel produced by laser powder bed fusion via in-process surface integrity improvement and phase change induced compressive residual stresses. *Additive Manufacturing* 88:104263. https://doi.org/10.1016/j.addma.2024.104263

[20] Zaba K, Szymański K, Balcerzak M, Różycka I, Kuczek Ł, Żabiński P (2024) Effect of Surface Finishing on the Corrosion Resistivity of 3D Printed M300 Steel. *Materials* 17(24):6047. https://doi.org/10.3390/ma17246047

[21] Song J, Tang Q, Chen H, Zhang Z, Feng Q, Zhao M, Ma S, Setchi R (2022) Laser powder bed fusion of high-strength maraging steel with concurrently enhanced strength and ductility after heat treatments. *Materials Science and Engineering: A* 854:143818. https://doi.org/10.1016/j.msea.2022.143818

[22] Mechali A, Hlinka J, Hajnys J, Cegan T, Zelinka J, Mesicek J, Sajgalik M, Petru J (2025) Research about SLM 3D printing-M300 maraging steel surface and post-processing characteristics. *Int J Adv Manuf Technol* 138(2):709–724. https://doi.org/10.1007/s00170-025-15413-1

[23] Mateev V, Sinico M, Gorji Ghalamestani S, Van Hooreweder B (2025) Magnetic properties of as-built and heat treated M789 and M300 maraging steels produced via laser powder bed fusion. *Next Materials* 6:100287. https://doi.org/10.1016/j.nxmate.2024.100287

[24] Turk C, Zunko H, Aumayr C, Leitner H, Kapp M (2019) Advances in Maraging Steels for Additive Manufacturing. *Berg Huettenmaenn Monatsh* 164(3):112–116. https://doi.org/10.1007/s00501-019-0835-z

[25] Perwitz JD (2020) *Study on Development of the Selective Laser Melting (SLM) Process Parameters for a Novel Specialized Cr-Ni Steel Powder "AMPO M789"*. Thesis - Diplomarbeit Institut für Fertigungstechnik und Photonische Technologien, . 20.500.12708/79525 Available at http://hdl.handle.net/20.500.12708/79525.

[26] Palad RB (2021) *Materials Characterization of M789 Steel Manufactured by Laser Powder Bed Fusion* Master's thesis The University of New Brunswick. Available at https://unbscholar.lib.unb.ca/handle/1882/13201.

[27] Cenalmor SB (2022) *Heat Treatment Effect on Mechanical Properties and Corrosion Behavior of DED Produced M789 Alloy* Master's thesis Incheon National University.
[28] Lek YZ (2024) *Additive Manufacturing of High-Strength Alloys for Marine and Offshore Applications*. Doctoral Thesis Nanyan Technological University, .
[29] Nyamuchiwa K (2024) *Laser Powder Bed Fusion of M789 on N709 Steel Substrate: Characterization of Mechanical and Microstructural Properties*. Doctoral Thesis The University of New Brunswick, . Available at https://unbscholar.lib.unb.ca/handle/1882/38073.
[30] Ordnung D (2025) *Development of New Strategies for Improving Precision and Mechanical Performance of Metal Parts Produced by Laser Powder Bed Fusion*. Doctoral Thesis, KU Leuven. Available at https://lirias.kuleuven.be/4222241&lang=en.
[31] Sinico M (2025) *Advancing Laser Powder Bed Fusion for Direct Metal Tooling Applications*. Doctoral Thesis KU Leuven, . Available at https://research.kuleuven.be/portal/en/project/3E171000.
[32] Kulkarni P, Magikar A, Pendse T (2020) A Practical Approach to Camera Calibration for Part Alignment for Hybrid Additive Manufacturing Using Computer Vision. *Intelligent Manufacturing and Energy Sustainability*, eds Reddy A, Marla D, Simic M, Favorskaya MN, Satapathy SC (Springer Singapore, Singapore), Vol. 169, pp 221–229. https://doi.org/10.1007/978-981-15-1616-0_21
[33] Metelkova J, Paggi U, Marco I, Sinico M, Thijs L, Van Hooreweder B (2023) Mould manufacturing by hybrid laser powder bed fusion of M789 steel on a functional base. *Joint Special Interest Group Meeting between Euspen and ASPE Advancing Precision in Additive Manufacturing* (euspen, KU Leuven), pp 78–81. Available at https://www.euspen.eu/events/sig-meeting-advancing-precision-in-additive-manufacturing-september-2023/?subid=sig-meeting-advancing-precision-in-additive-manufacturing-september-2023.
[34] Palad R, Tian Y, Chadha K, Rodrigues S, Aranas C (2020) Microstructural features of novel corrosion-resistant maraging steel manufactured by laser powder bed fusion. *Materials Letters* 275:128026. https://doi.org/10.1016/j.matlet.2020.128026
[35] Tian Y, Palad R, Aranas C (2020) Microstructural evolution and mechanical properties of a newly designed steel fabricated by laser powder bed fusion. *Additive Manufacturing* 36:101495. https://doi.org/10.1016/j.addma.2020.101495
[36] Nyamuchiwa K, Pasco J, McCarthy T, Keshavarzkermani A, Wang T, Aranas C (2024) Analysis of dynamic recrystallization through austenite grain reconstruction of additively manufactured martensitic M789 steel. *Materials Science and Engineering: A* 897:146345. https://doi.org/10.1016/j.msea.2024.146345
[37] Brytan Z, Król M, Benedyk M, Pakieła W, Tański T, Dagnaw MJ, Snopiński P, Pagáč M, Czech A (2022) Microstructural and Mechanical Properties of Novel Co-Free Maraging Steel M789 Prepared by Additive Manufacturing. *Materials* 15(5):1734. https://doi.org/10.3390/ma15051734
[38] Tian Y, Nyamuchiwa K, Chadha K, He Y, Aranas C (2022) Laser powder bed fusion of M789 maraging steel on Cr–Mo N709 steel: Microstructure, texture, and mechanical

properties. *Materials Science and Engineering: A* 839:142827. https://doi.org/10.1016/j.msea.2022.142827

[39] Laliberté-Riverin S, Yassine SR, Mena-Morcillo E, Sanni K, Cova M, Hassanipour M, Provencher PR, Mauzeroll J, Brochu M (2024) Microstructure, corrosion behavior, and fatigue resistance of laser powder bed fusion-produced precipitation-hardening martensitic M789 stainless steel. *Surfaces and Interfaces* 45:103830. https://doi.org/10.1016/j.surfin.2023.103830

[40] Sinico M, Metelkova J, Dalemans T, Thijs L, Van Hooreweder B (2022) High speed laser powder bed fusion of M789 tool steel with an optimized 120 µm layer thickness approach. *Procedia CIRP* 111:162–165. https://doi.org/10.1016/j.procir.2022.08.141

[41] Saville A, Benzing JT, Zhang F, Aroh JW, Weaver JS, Evans RC, Derimow N, Webster S, Hrabe N, Allen CR, Moser N, Martin ML, Holm J, Aumayr C, Seifert T, Hirtler M (2025) Priming Additively Manufactured Cobalt-free Maraging Steels for Improved Properties via Changes to As-Built Microstructure. *NIST Internal Report 8582* https://doi.org/10.6028/NIST.IR.8582

[42] Lek YZ, Wang C, Shen X, Chen Z, Ramamurty U, Zhou K (2022) Additive manufacturing of corrosion-resistant maraging steel M789 by directed energy deposition. *Materials Science and Engineering: A* 857:144032. https://doi.org/10.1016/j.msea.2022.144032

[43] Han SC, Chaudry UM, Cenalmor SB, Yeon SM, Yoon J, Lee H, Kim K, Jun TS (2023) Effect of Heat Treatment on Corrosion and Mechanical Properties of M789 Alloy Fabricated Using DED. *Metals* 13(7):1214. https://doi.org/10.3390/met13071214

[44] Tian Y, Palad R, Jiang L, Dorin T, Chadha K, Aranas C (2021) The effect of heat treatments on mechanical properties of M789 steel fabricated by laser powder bed fusion. *Journal of Alloys and Compounds* 885:161033. https://doi.org/10.1016/j.jallcom.2021.161033

[45] ASTM E8/E8M-24 (2024) Test Methods for Tension Testing of Metallic Materials. https://doi.org/10.1520/E0008_E0008M-24.

[46] Dzugan J, Lucon E, Koukolikova M, Li Y, Rzepa S, Yasin M, Shao S, Shamsaei N, Seifi M, Lodeiro M, Lefebvre F, Mayer U, Olbricht J, Houska M, Mentl V, You Z (2024) ASTM interlaboratory study on tensile testing of AM deposited and wrought steel using miniature specimens. *Theoretical and Applied Fracture Mechanics* 131:104410. https://doi.org/10.1016/j.tafmec.2024.104410

[47] Ku H (1966) Notes on the use of propagation of error formulas. *J RES NATL BUR STAN SECT C ENG INSTR* 70C(4):263. https://doi.org/10.6028/jres.070C.025

[48] Atkinson HV, Davies S (2000) Fundamental aspects of hot isostatic pressing: An overview. *Metall Mater Trans A* 31(12):2981–3000. https://doi.org/10.1007/s11661-000-0078-2

Appendix A. Engineering Stress-Strain Curves

The engineering stress-strain curves are presented in this section. Note, the data has been filtered to exclude tests where the failure occurred outside of the measurement portion of the physical extensometer. The *MT#* label stands for 'mechanical test number' that was used for internal tracking. The colors in this section are ordered per-test, and do not correlate with the color scheme defined in the main portion of the report.

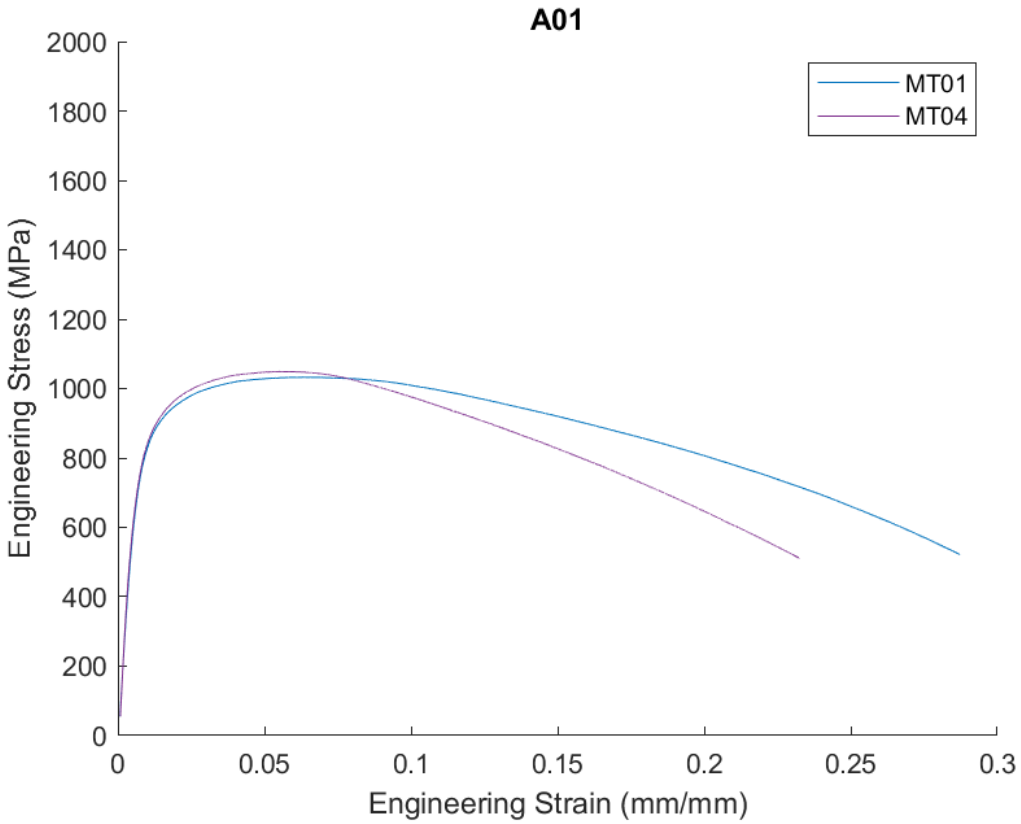

Fig. A1. Engineering stress-strain curves for the A01 condition.

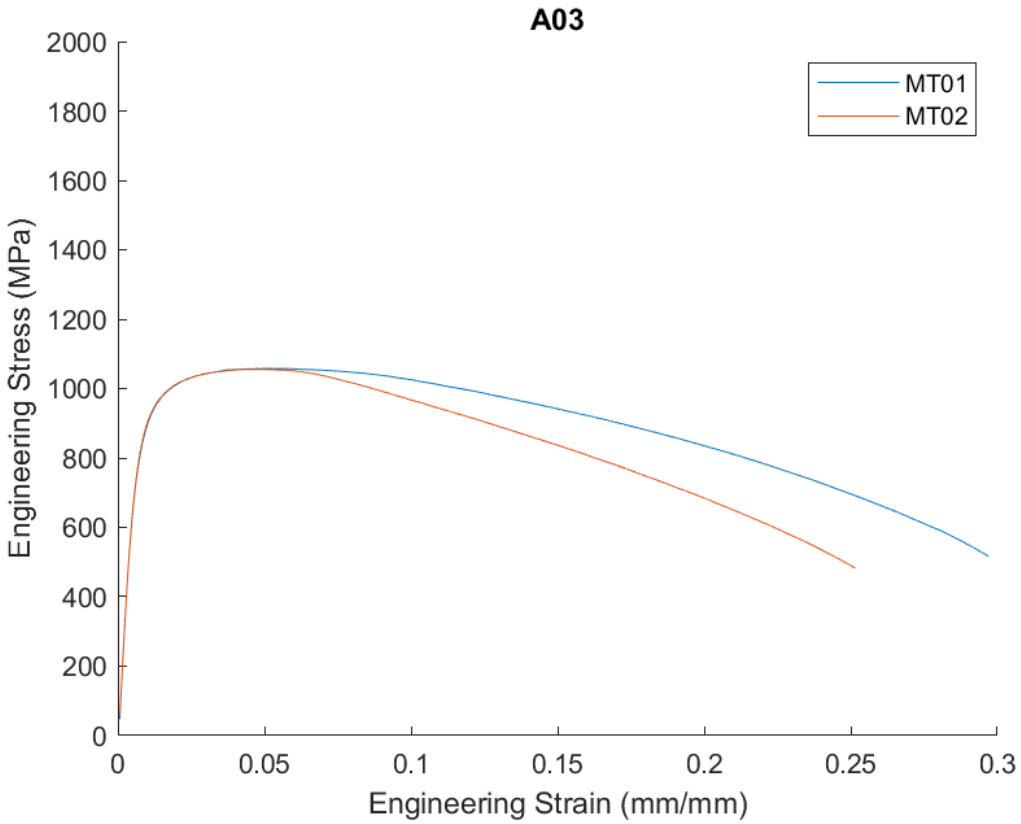

Fig. A2. Engineering stress-strain curves for the A03 condition.

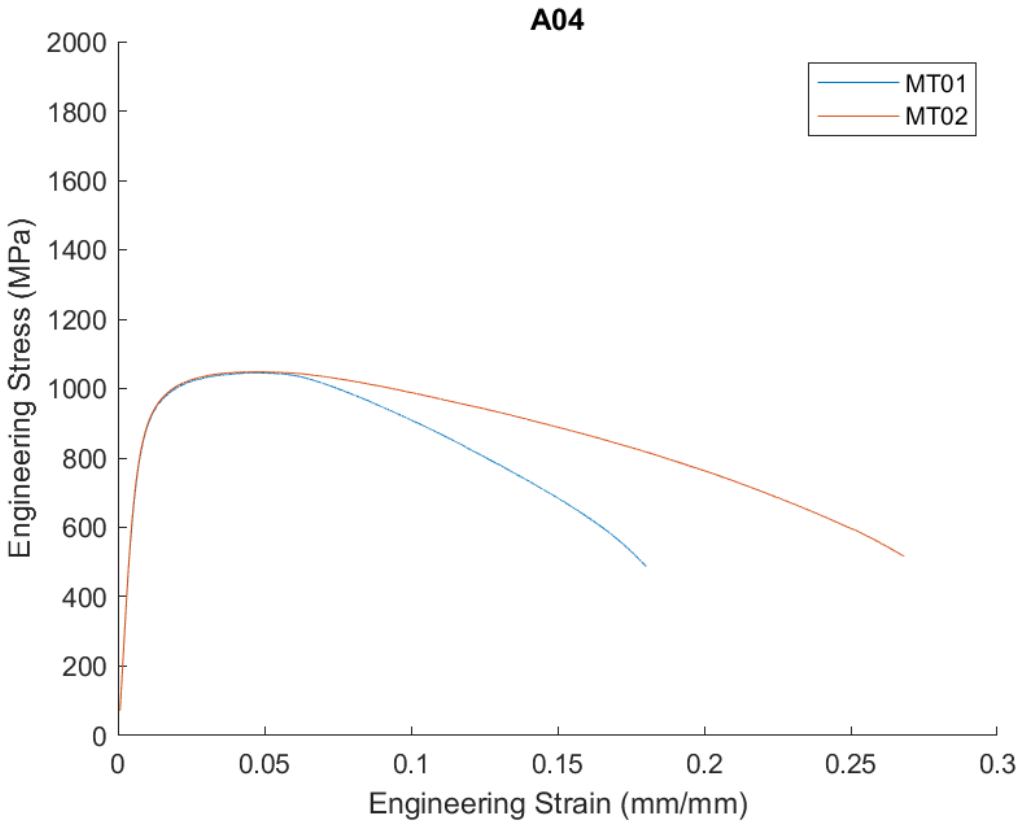

Fig. A3. Engineering stress-strain curves for the A04 condition.

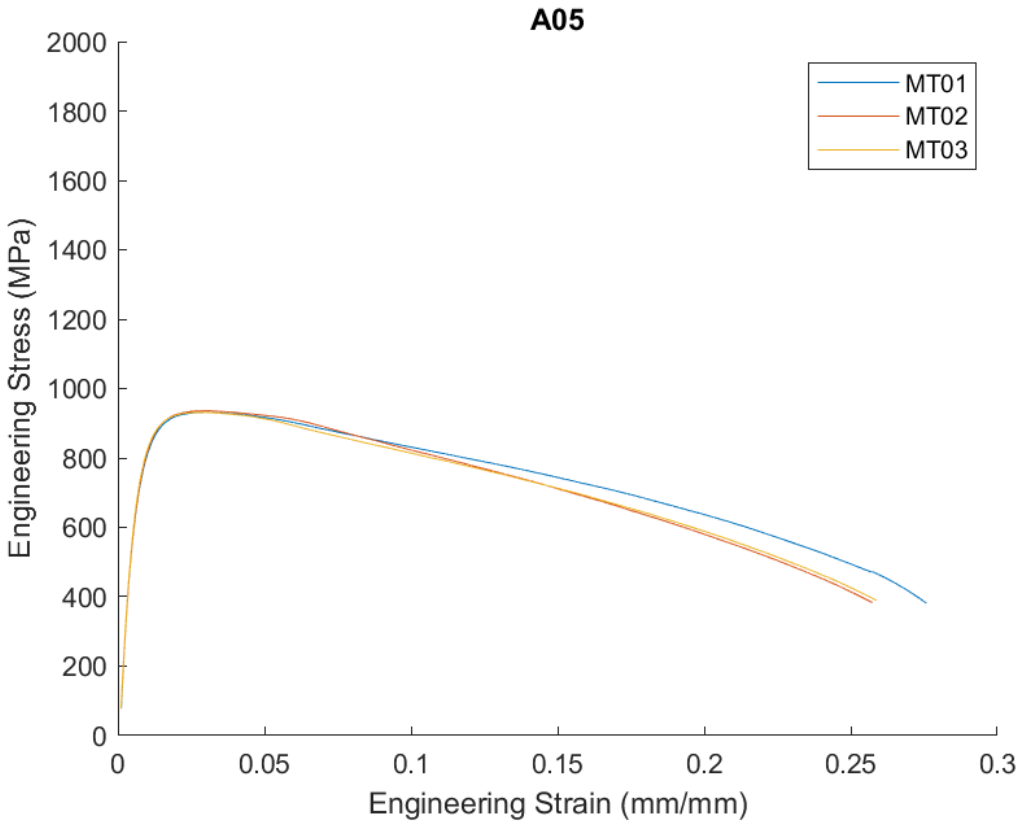

Fig. A4. Engineering stress-strain curves for the A05 condition.

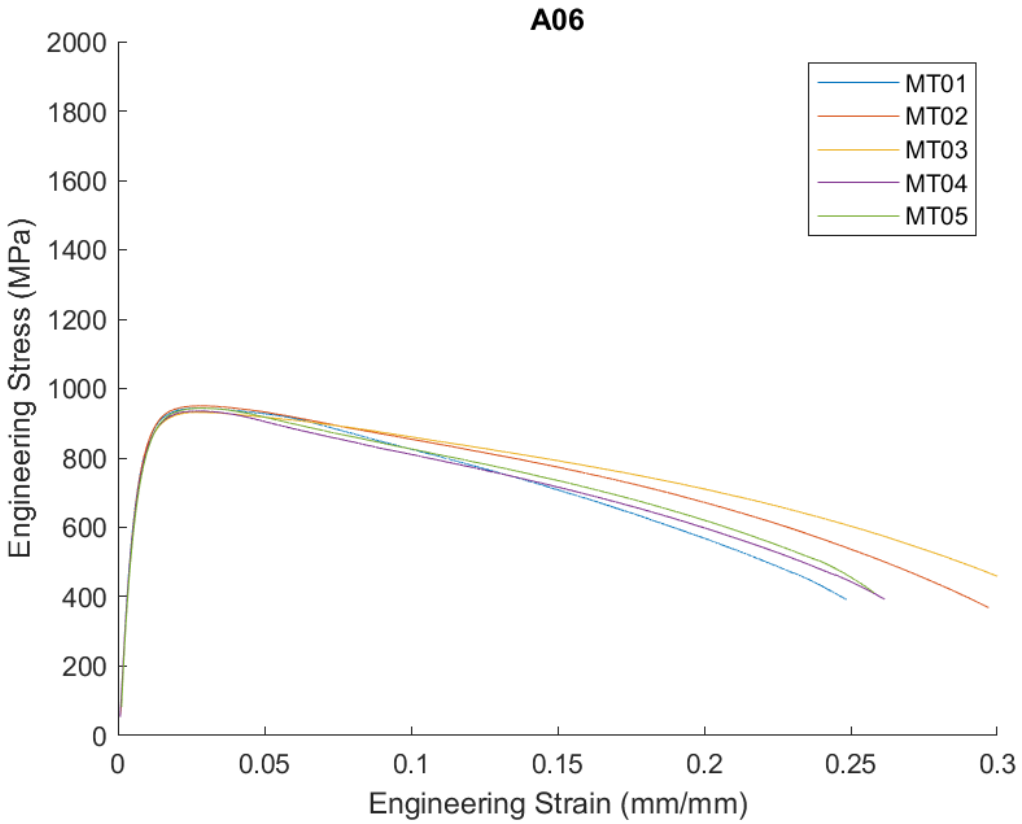

Fig. A5. Engineering stress-strain curves for the A06 condition.

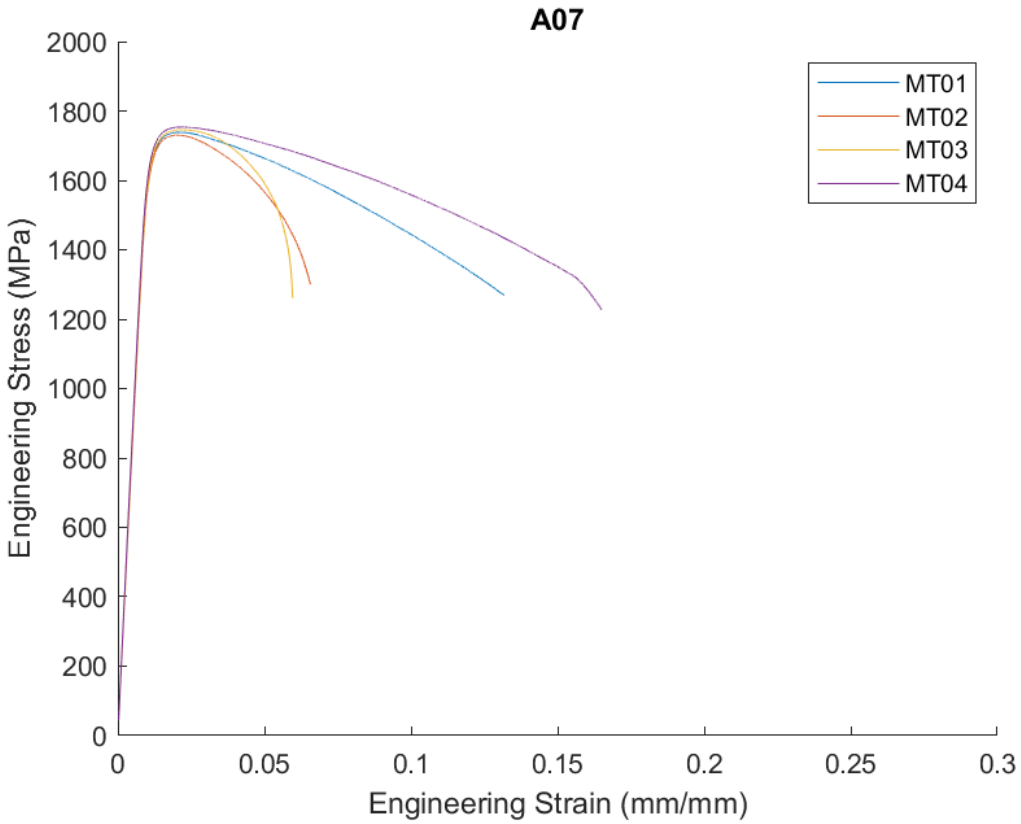

Fig. A6. Engineering stress-strain curves for the A07 condition.

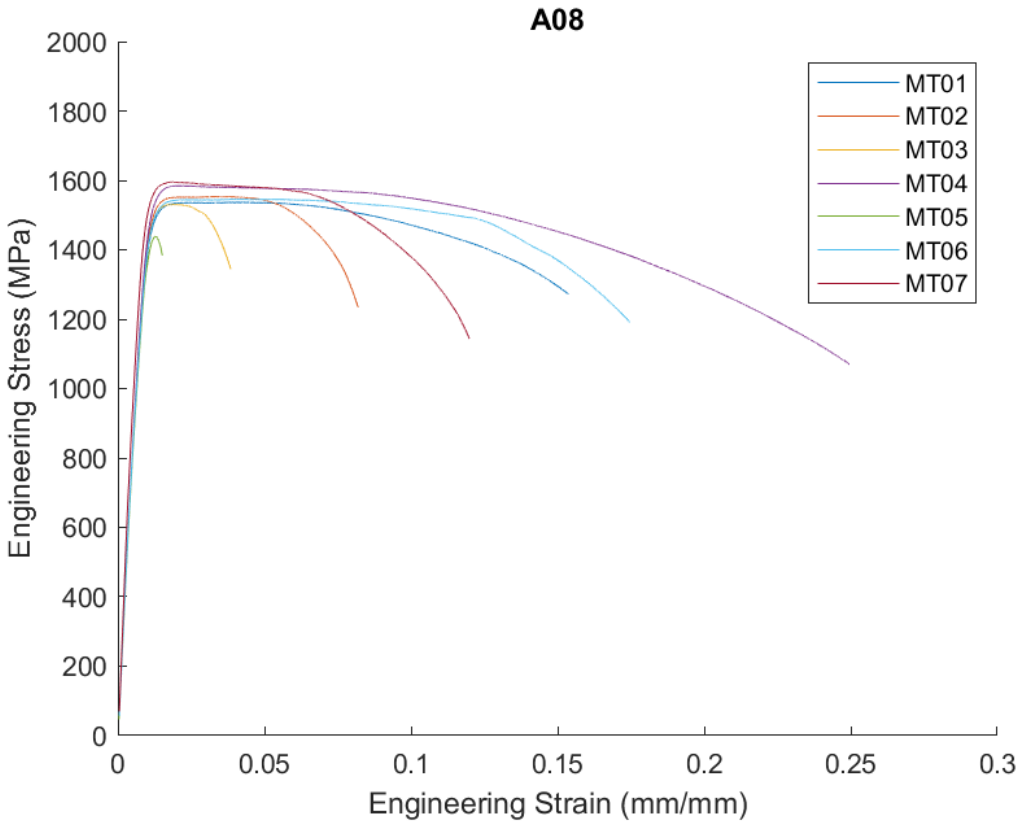

Fig. A7. Engineering stress-strain curves for the A08 condition.

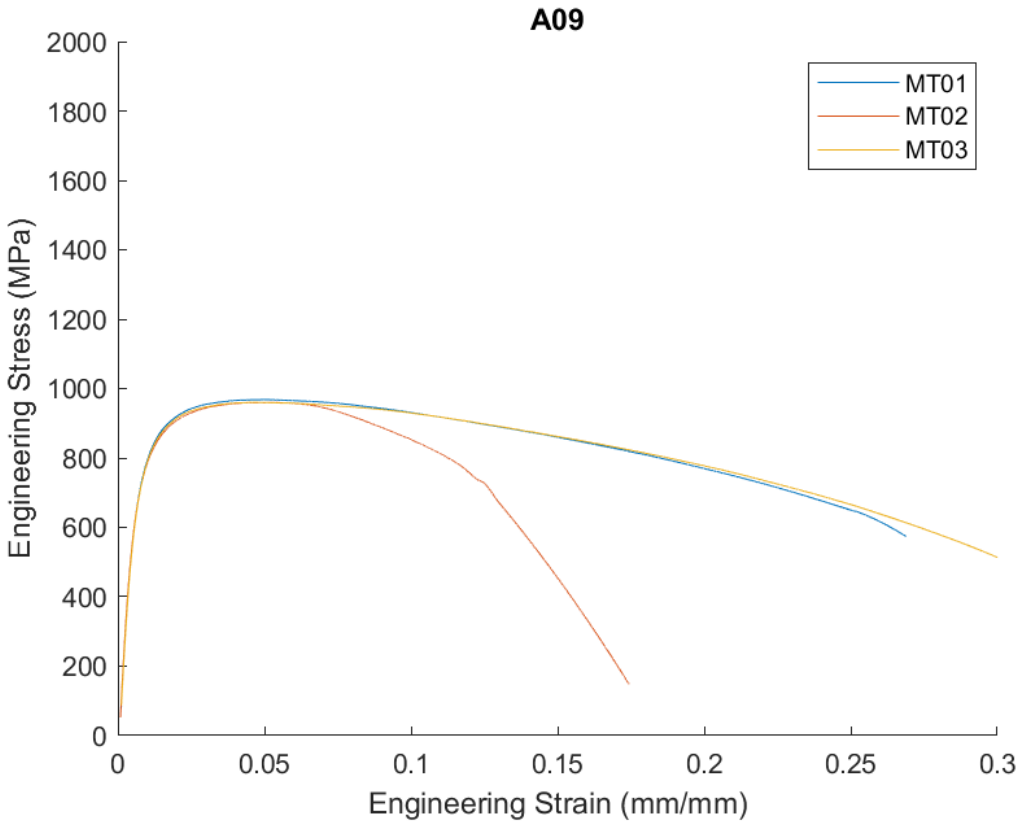

Fig. A8. Engineering stress-strain curves for the A09 condition.

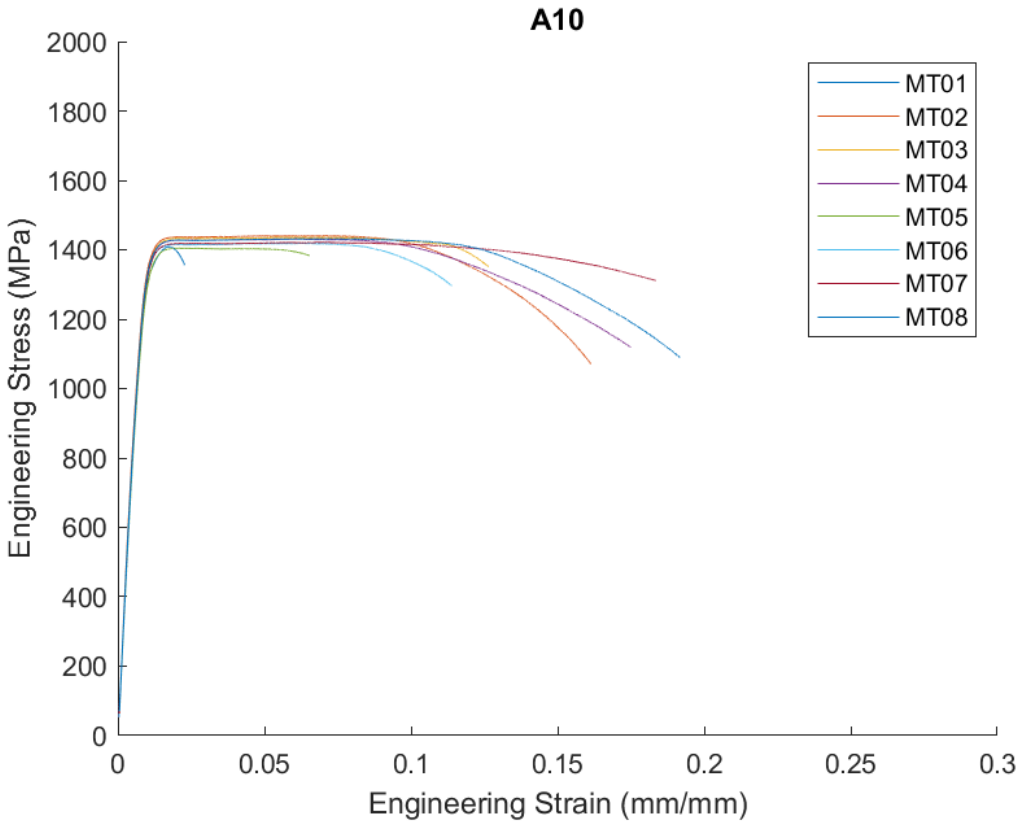

Fig. A9. Engineering stress-strain curves for the A10 condition.

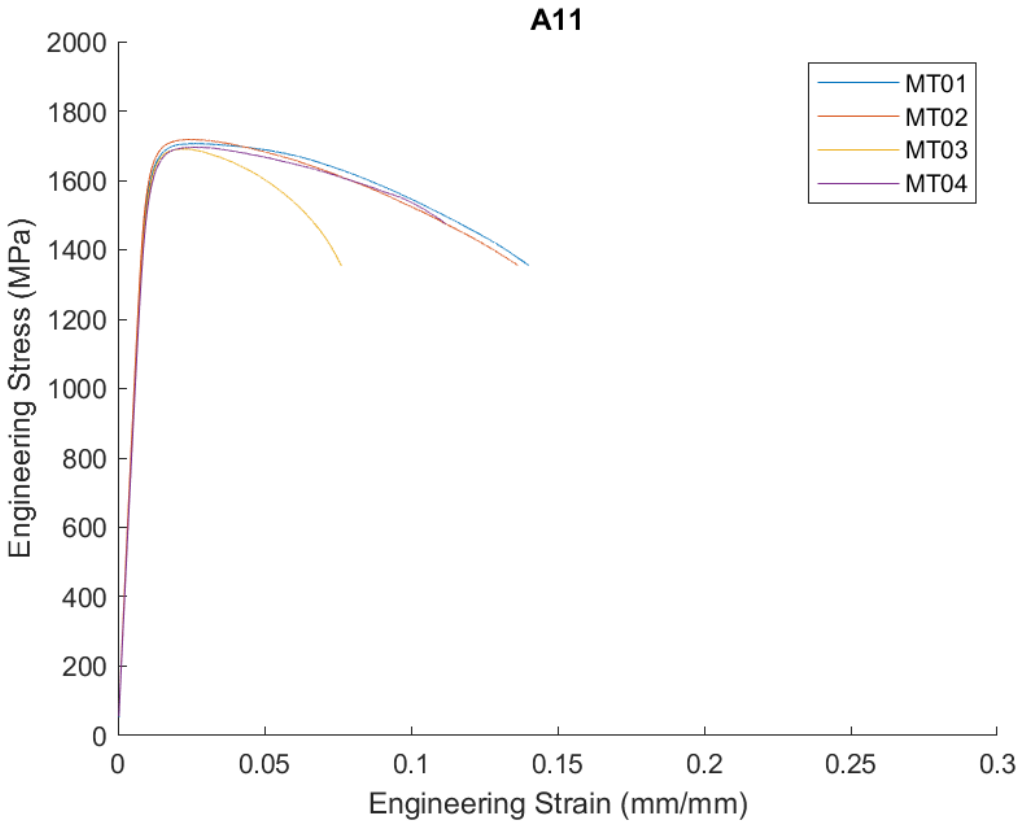

Fig. A10. Engineering stress-strain curves for the A11 condition.

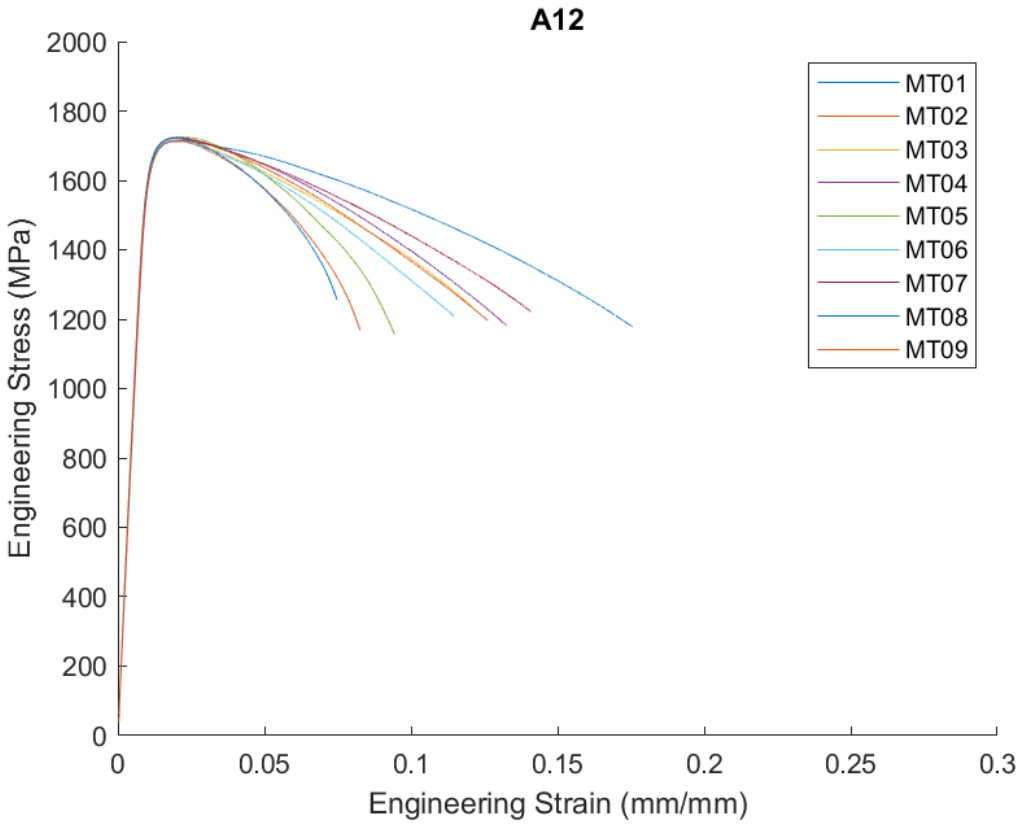

Fig. A11. Engineering stress-strain curves for the A12 condition.

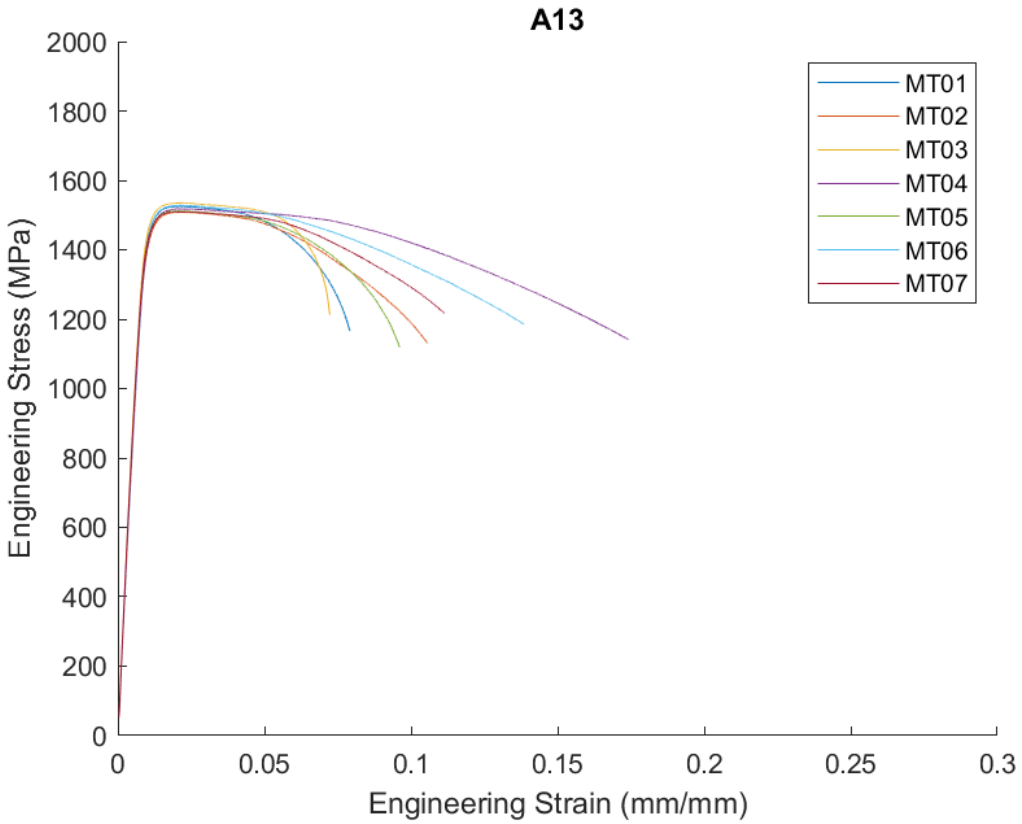

Fig. A12. Engineering stress-strain curves for the A13 condition.

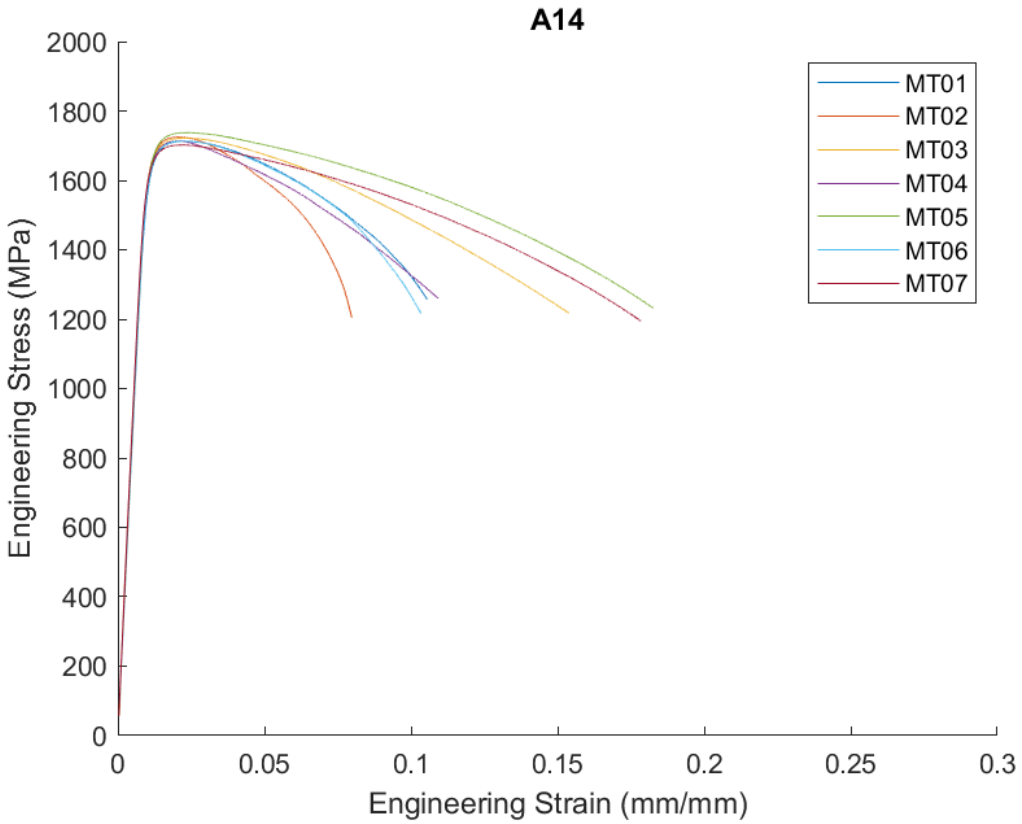

Fig. A13. Engineering stress-strain curves for the A14 condition.

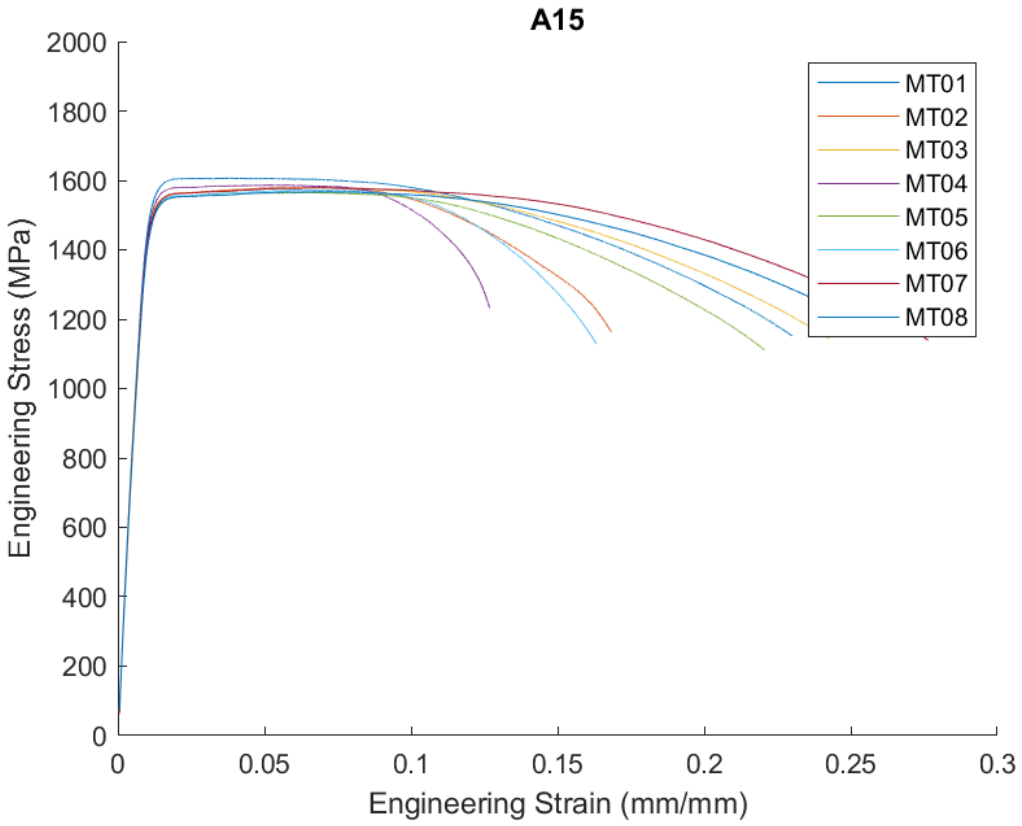

Fig. A14. Engineering stress-strain curves for the A15 condition.

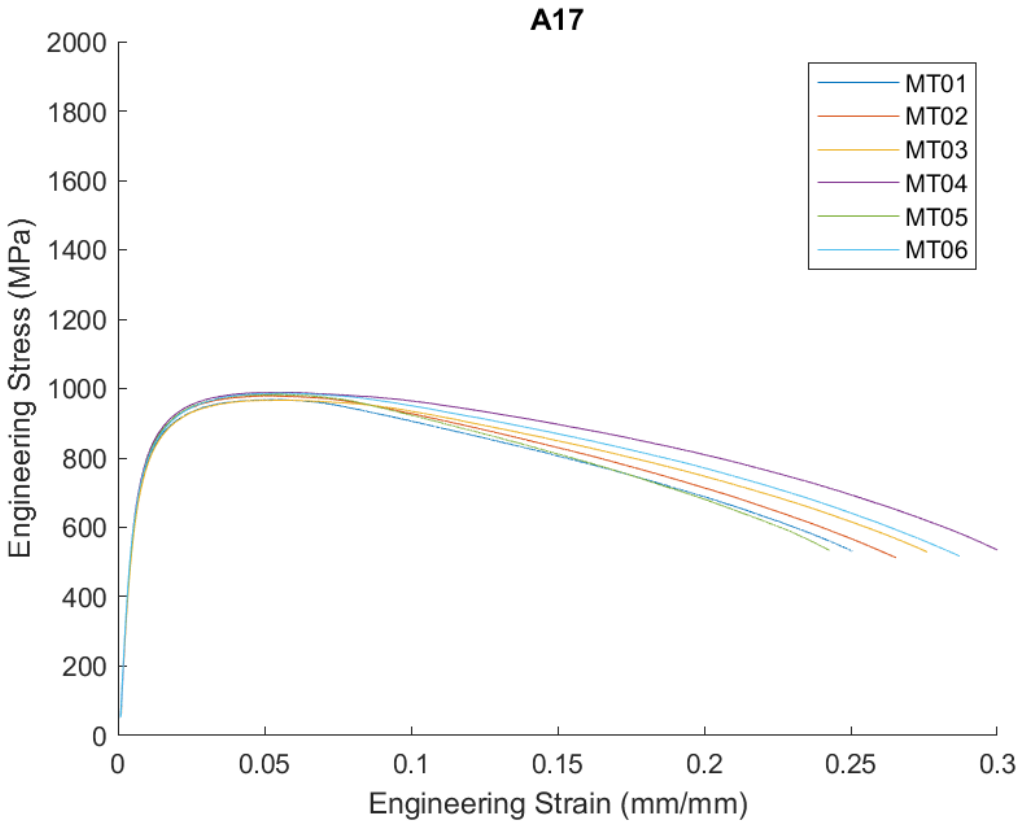

Fig. A15. Engineering stress-strain curves for the A17 condition.

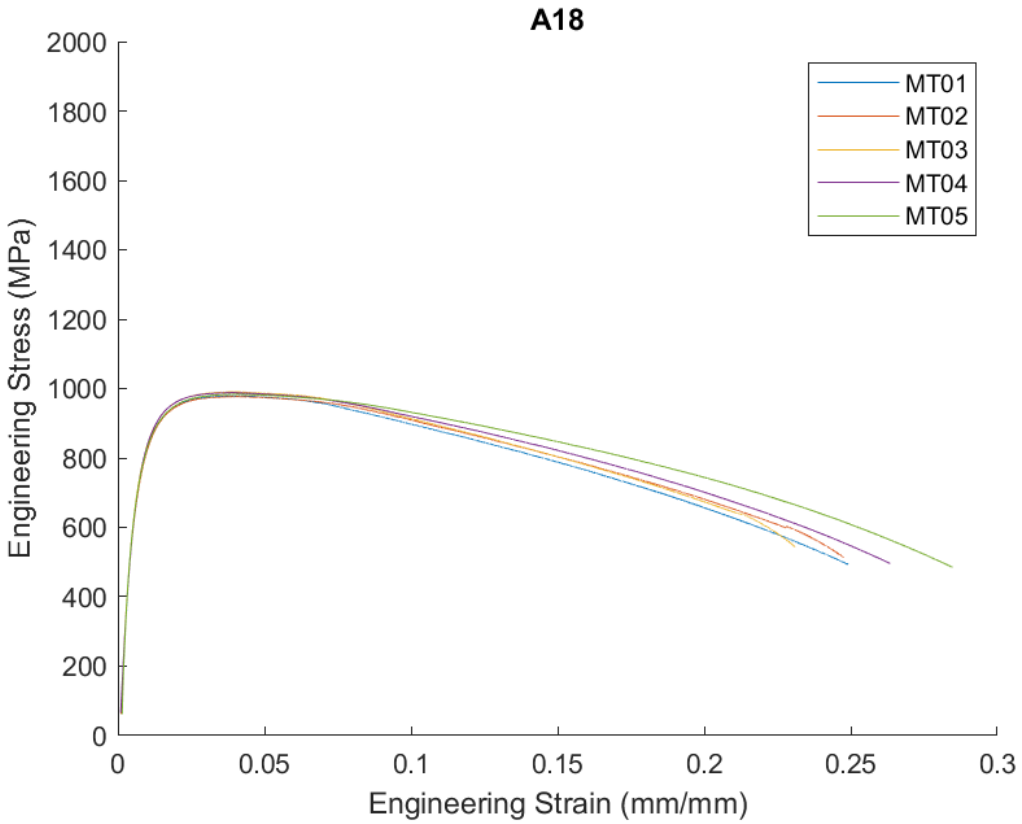

Fig. A16. Engineering stress-strain curves for the A18 condition.

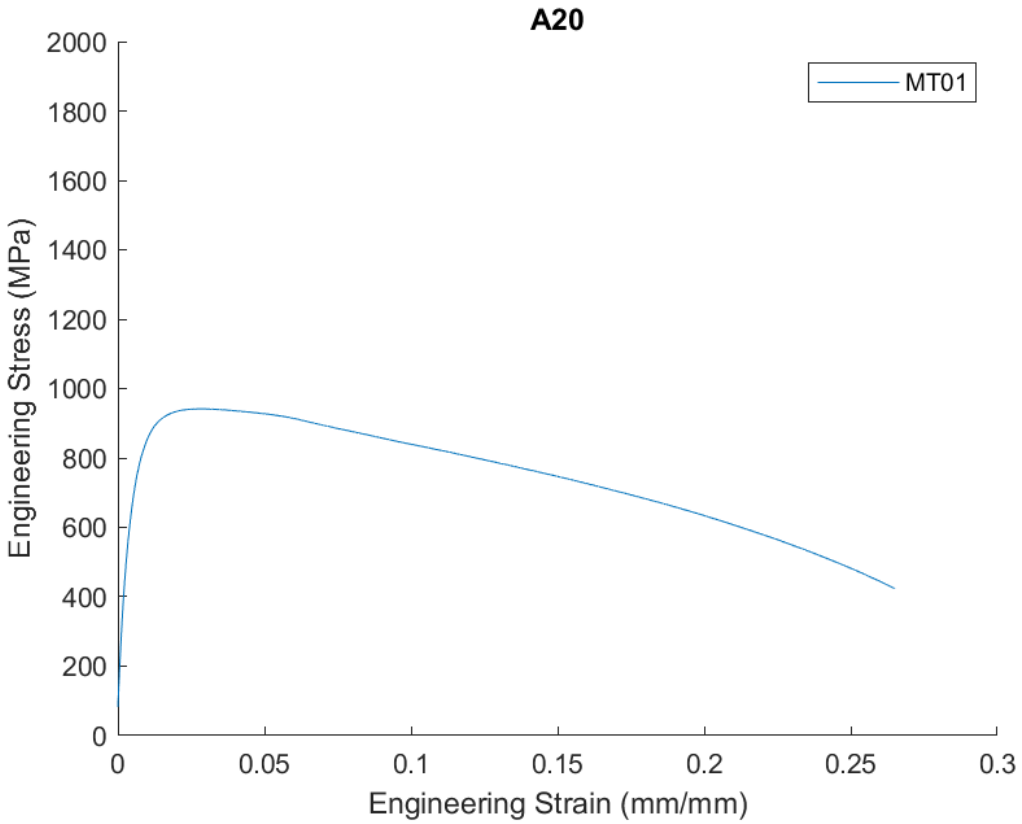

Fig. A17. Engineering stress-strain curves for the A20 condition.

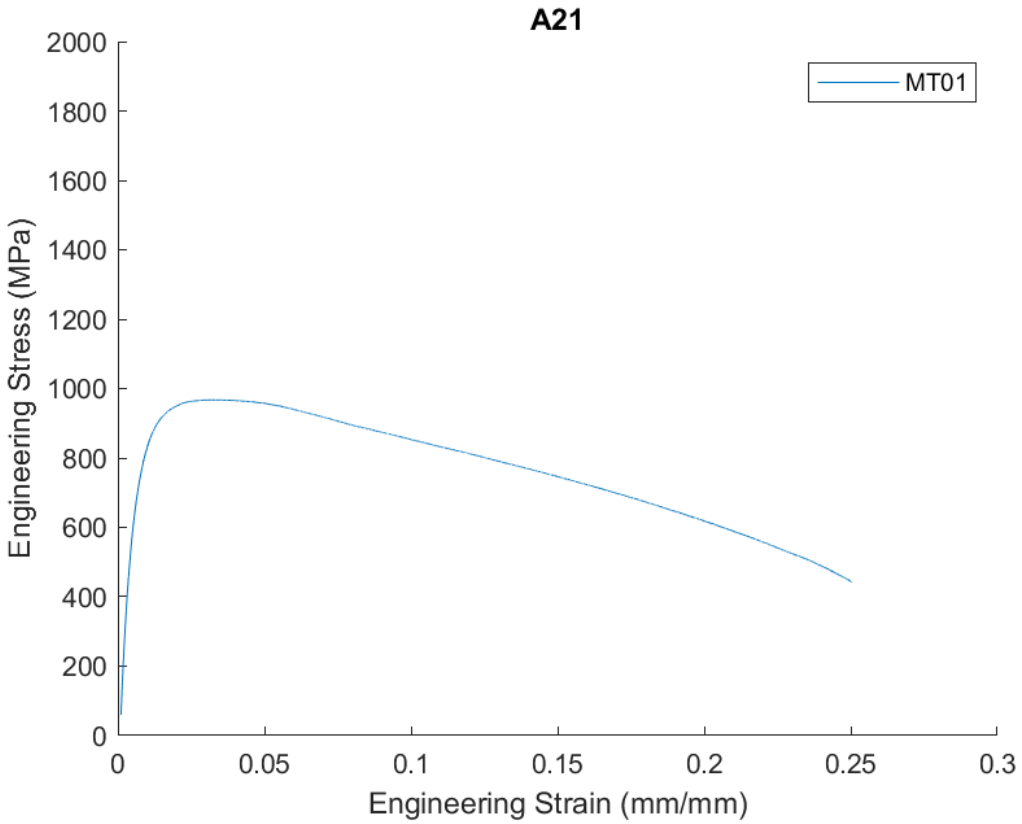

Fig. A18. Engineering stress-strain curves for the A21 condition.

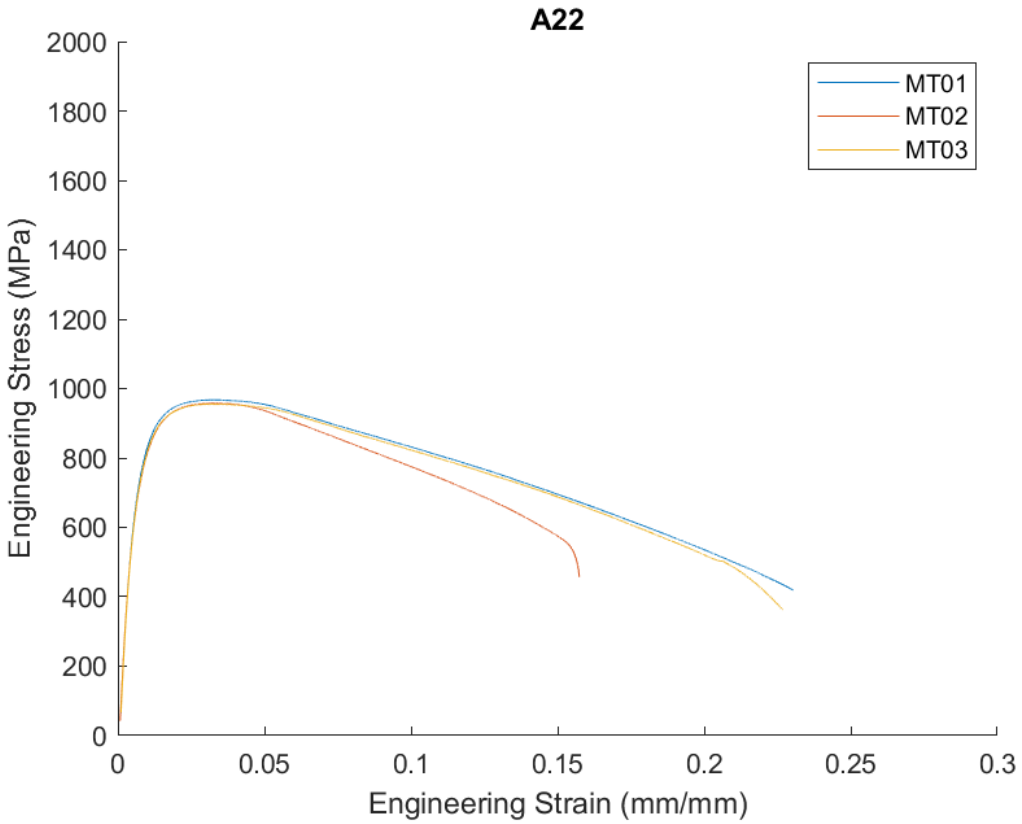

Fig. A19. Engineering stress-strain curves for the A22 condition.

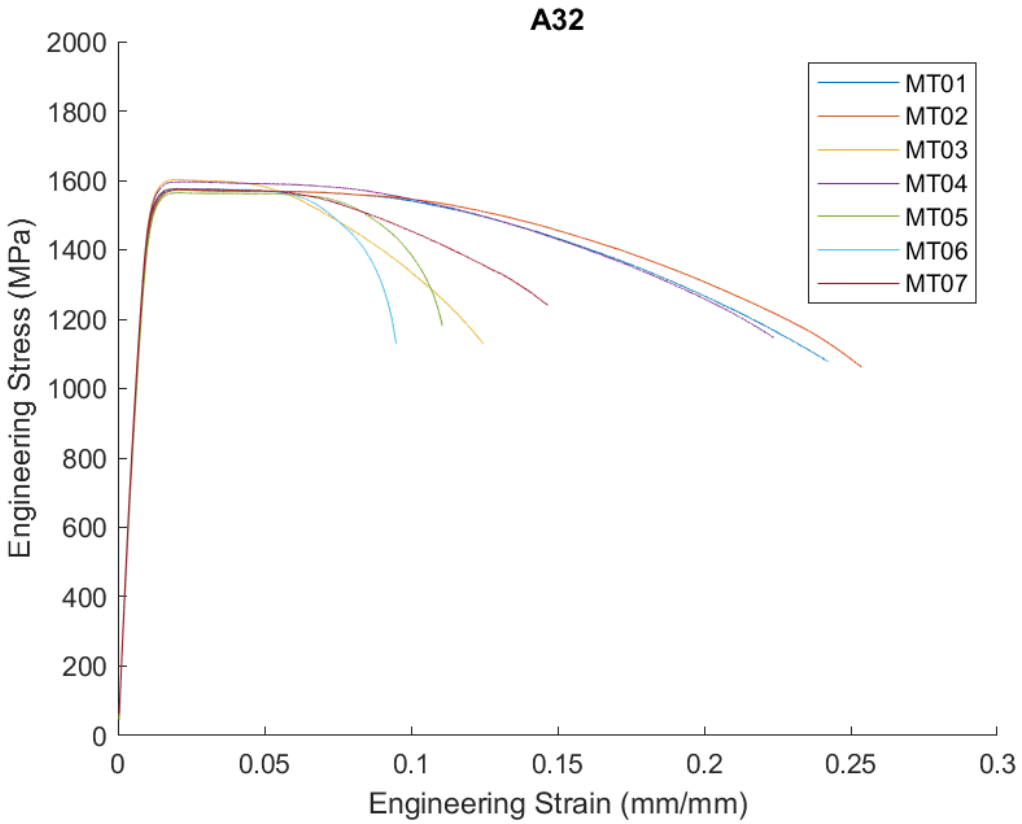

Fig. A20. Engineering stress-strain curves for the A32 condition.

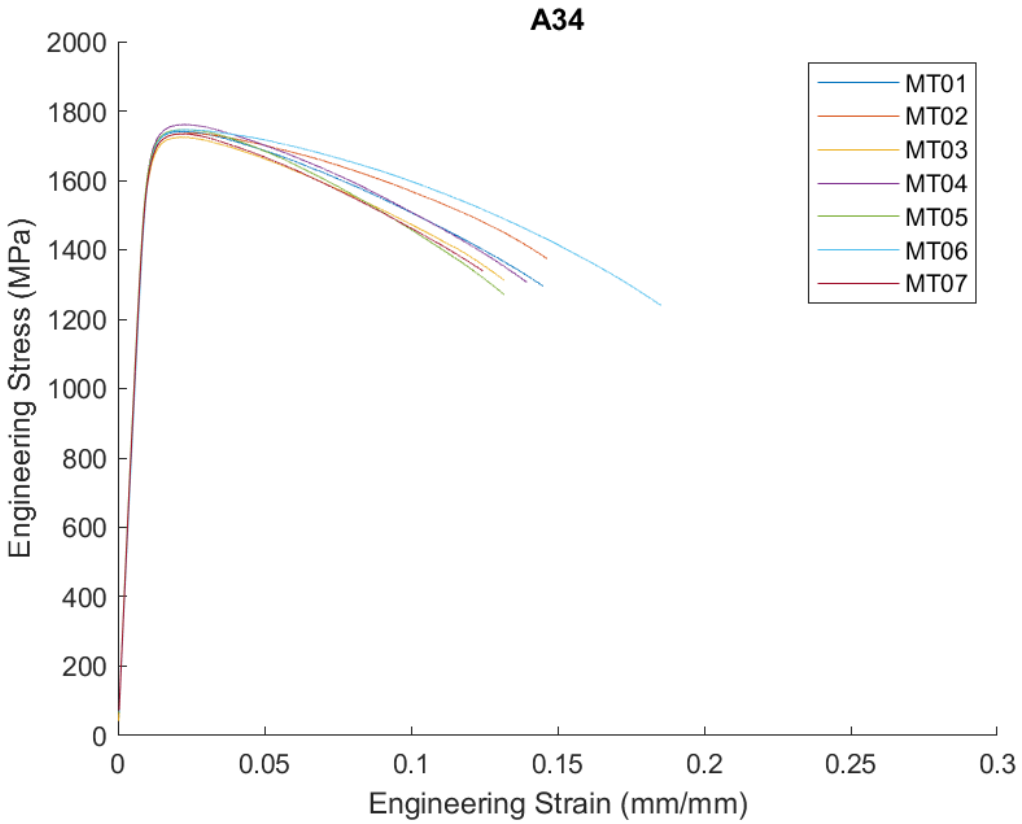

Fig. A21. Engineering stress-strain curves for the A34 condition.

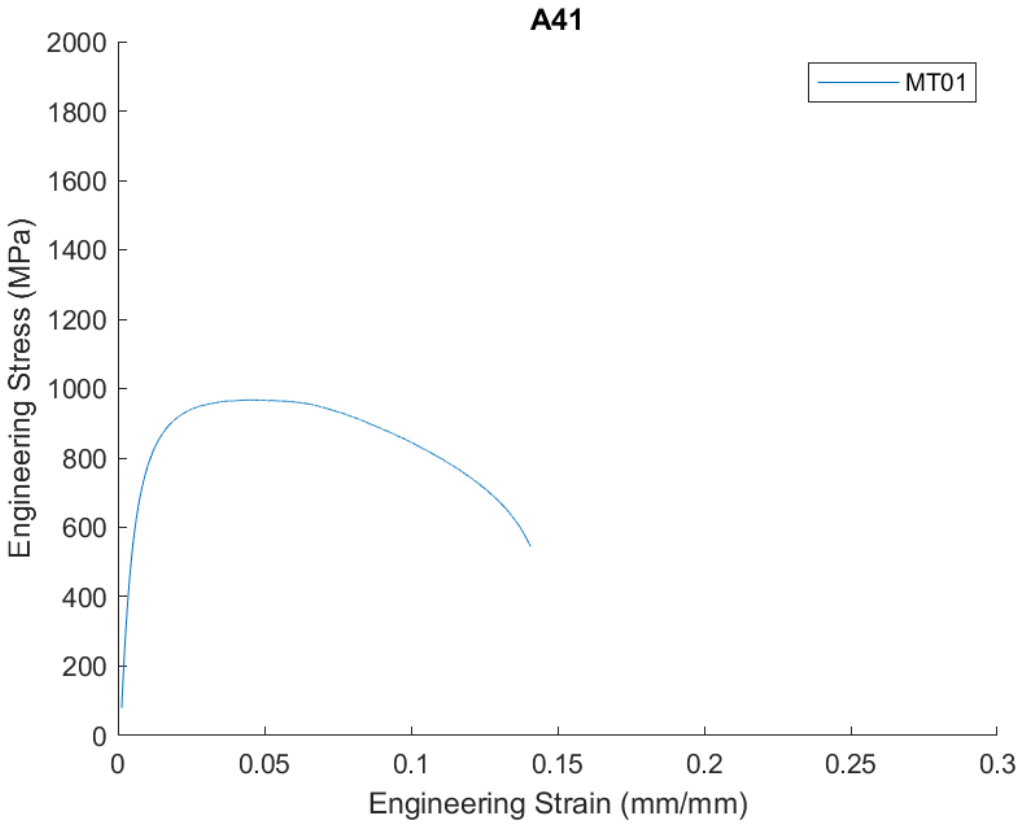

Fig. A22. Engineering stress-strain curves for the A41 condition.

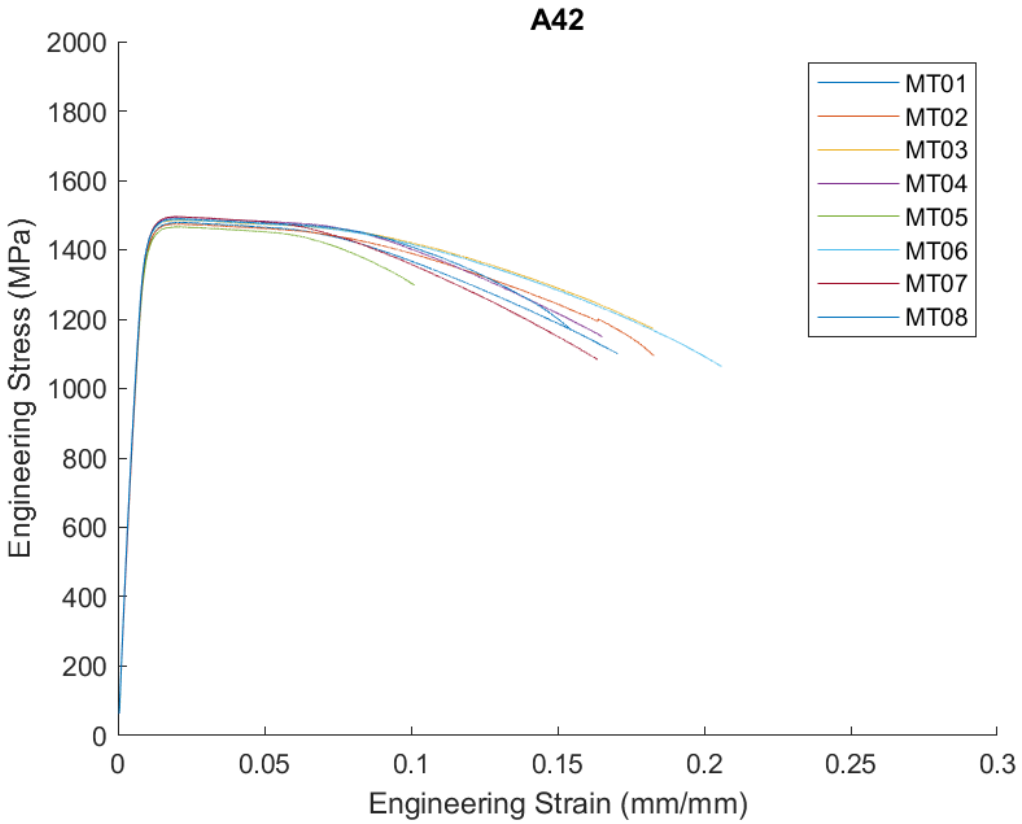

Fig. A23. Engineering stress-strain curves for the A42 condition.

Appendix B. True Stress-Strain Curves

The true stress-strain curves for the data are presented in this section. The *MT#* label stands for 'mechanical test number'. The colors in this section are per-test, and do not correlate with the color scheme defined in the main portion of the report.

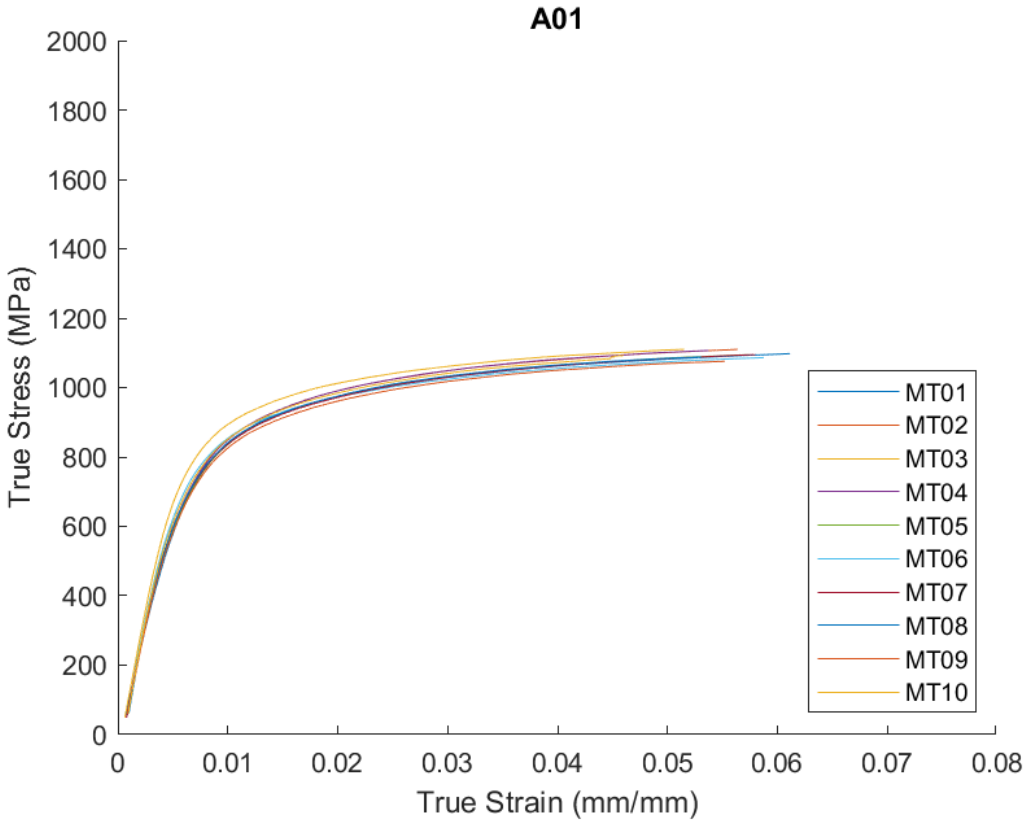

Fig. B1. True stress-strain curves for the A01 condition.

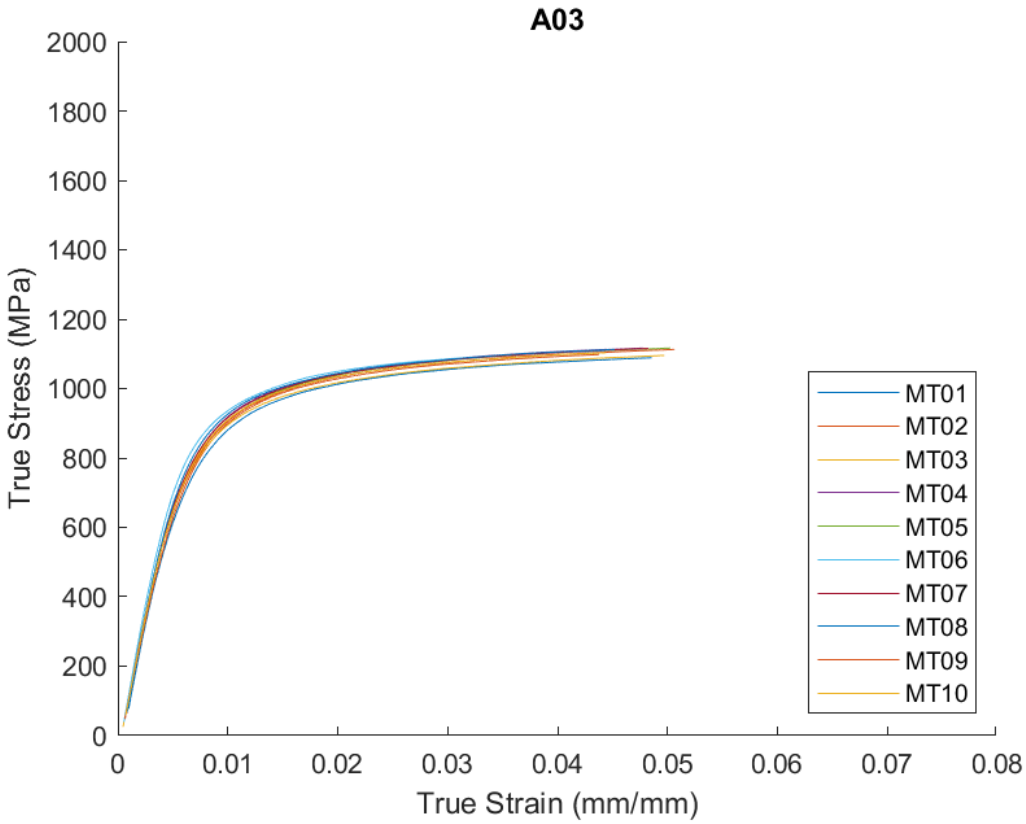

Fig. B2. True stress-strain curves for the A03 condition.

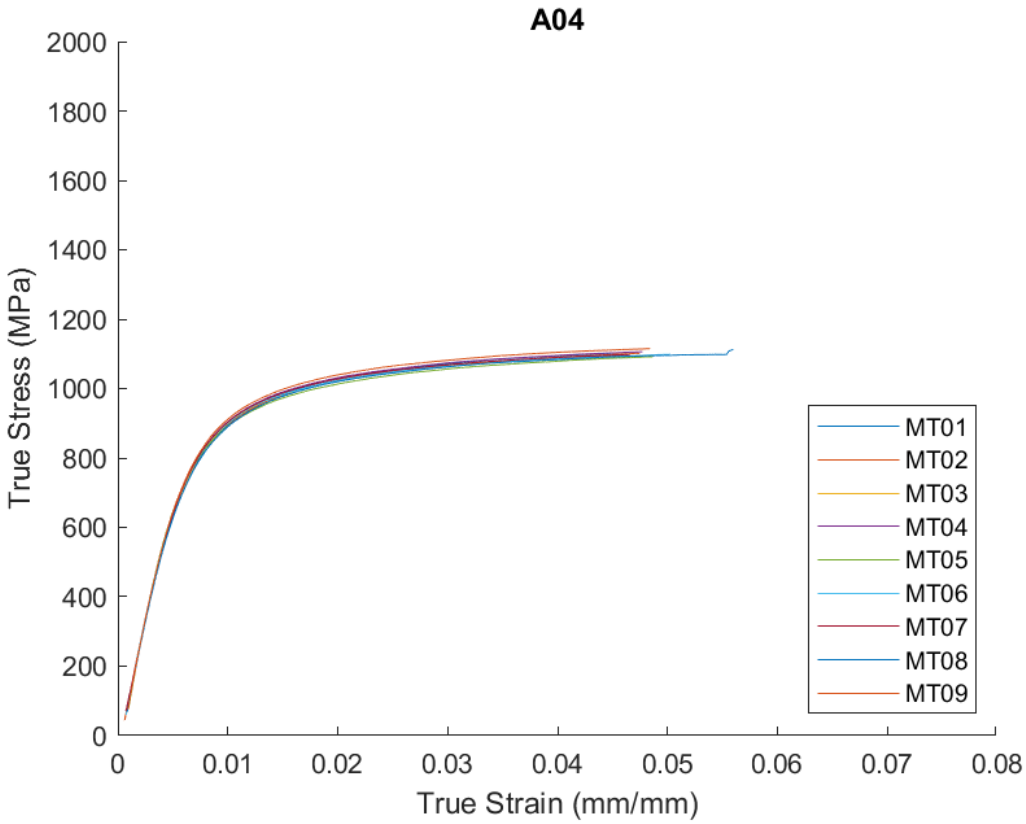

Fig. B3. True stress-strain curves for the A04 condition.

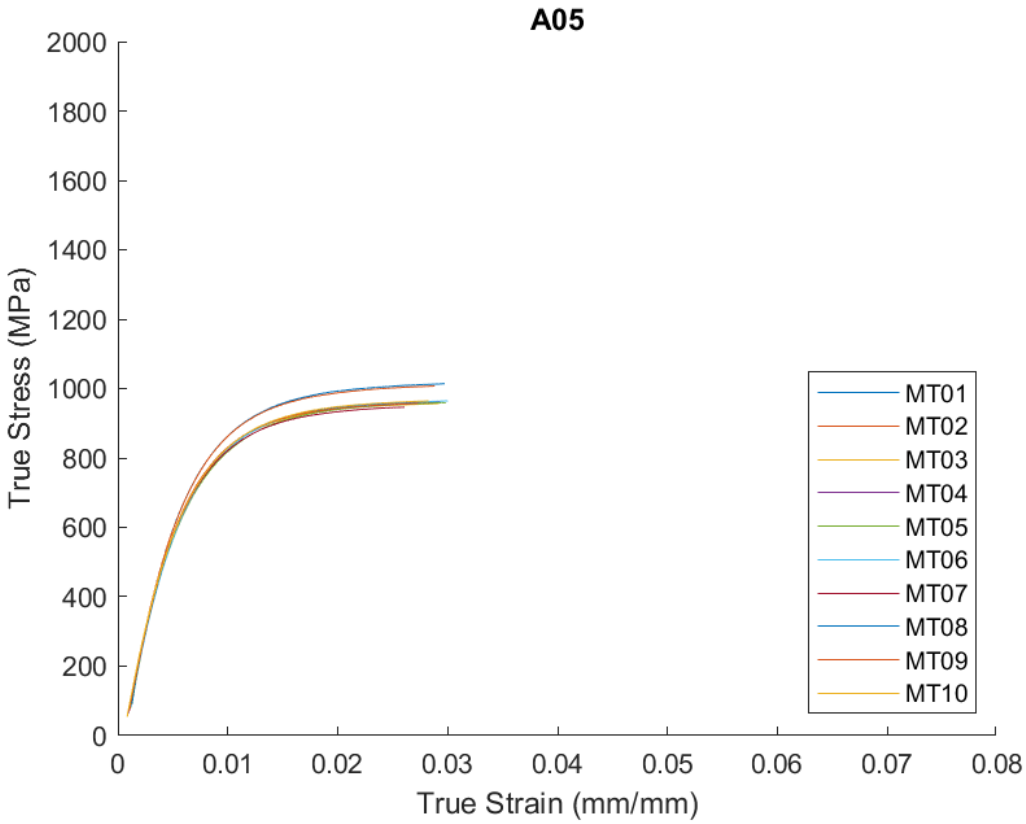

Fig. B4. True stress-strain curves for the A05 condition.

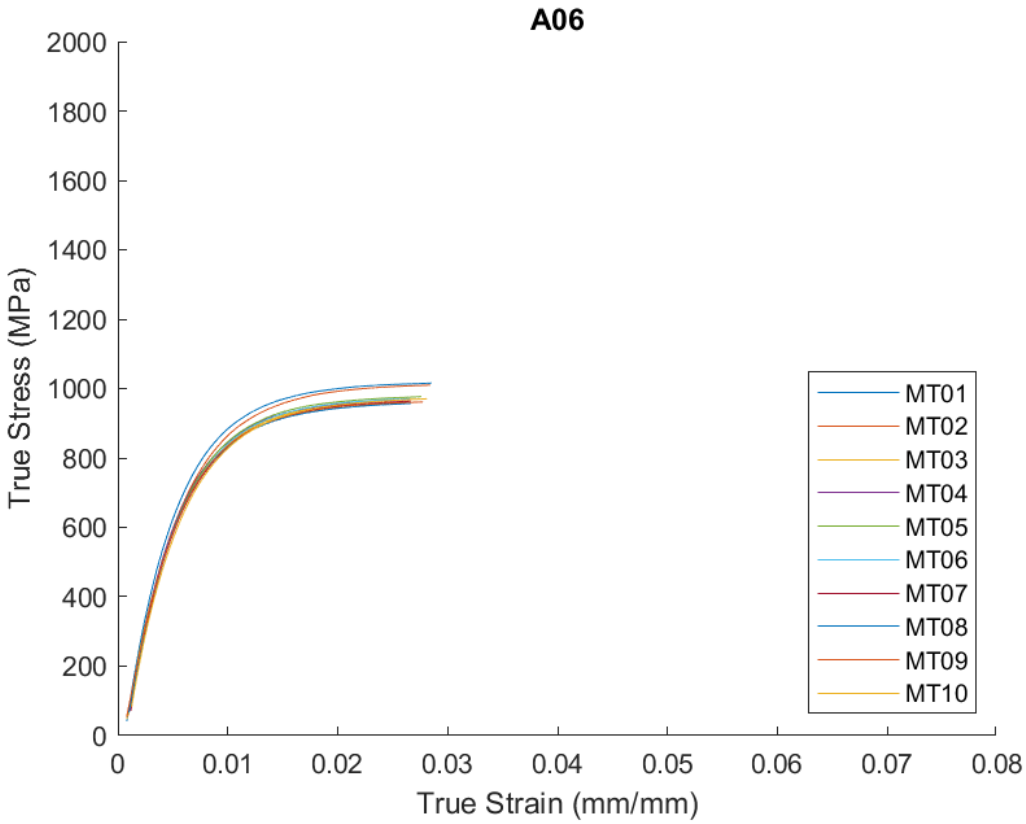

Fig. B5. True stress-strain curves for the A06 condition.

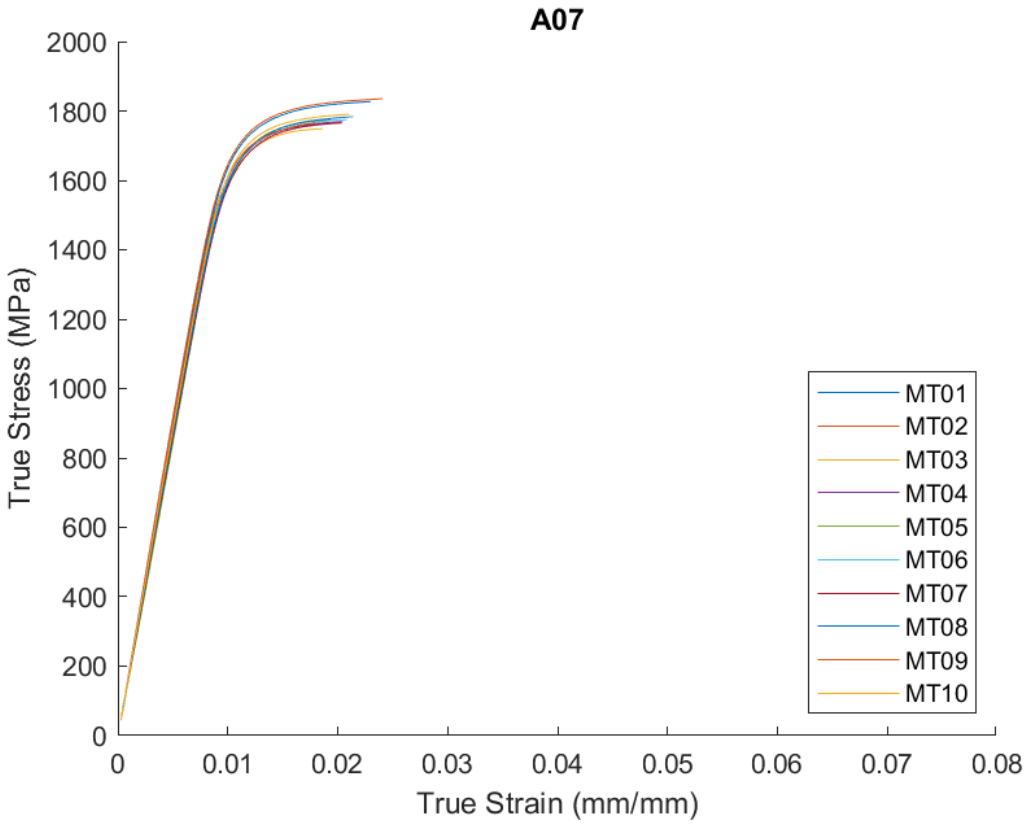

Fig. B6. True stress-strain curves for the A07 condition.

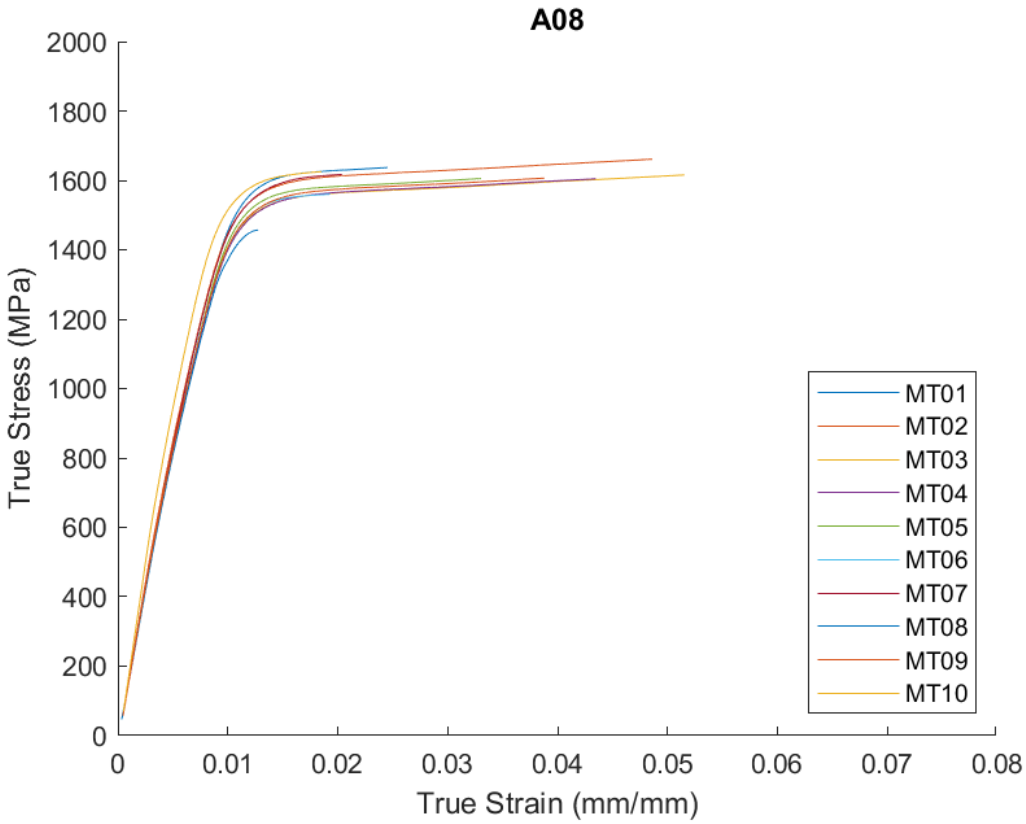

Fig. B7. True stress-strain curves for the A08 condition.

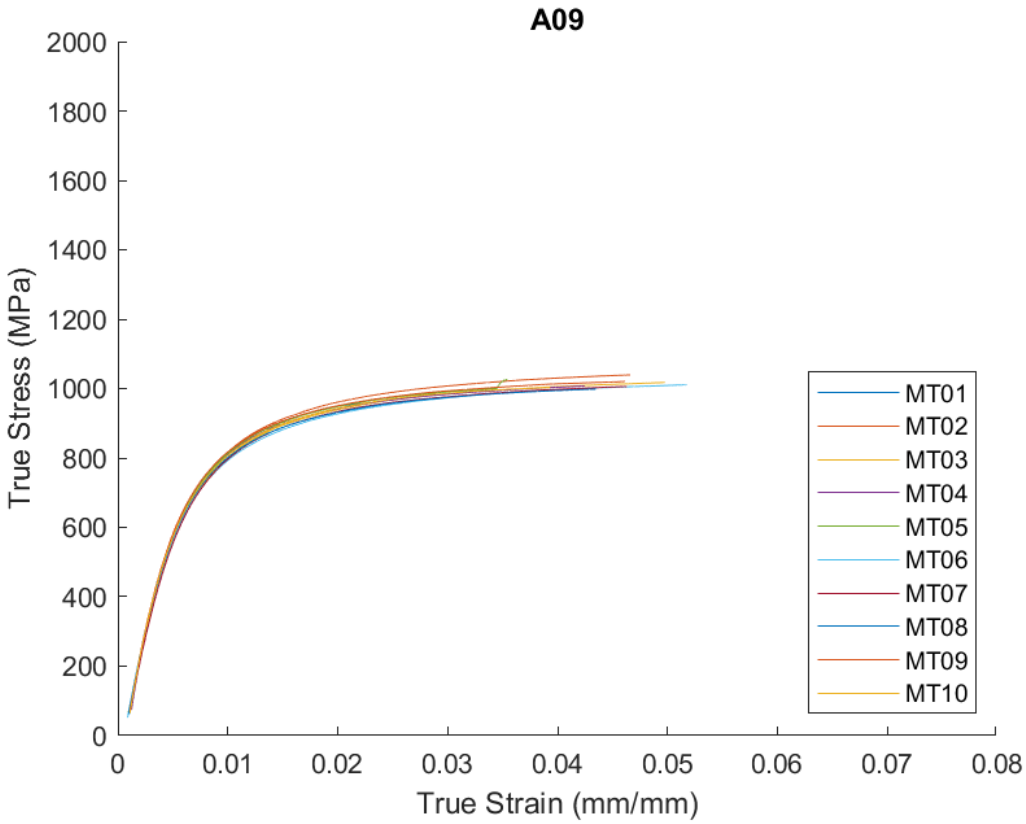

Fig. B8. True stress-strain curves for the A09 condition.

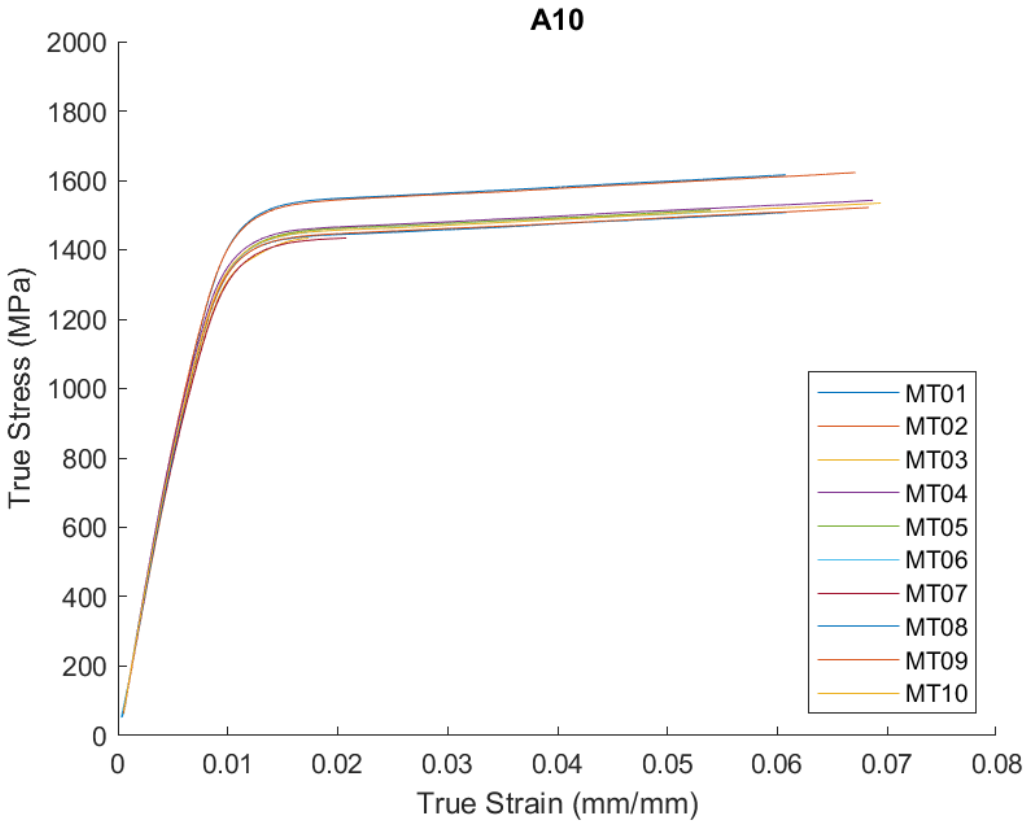

Fig. B9. True stress-strain curves for the A10 condition.

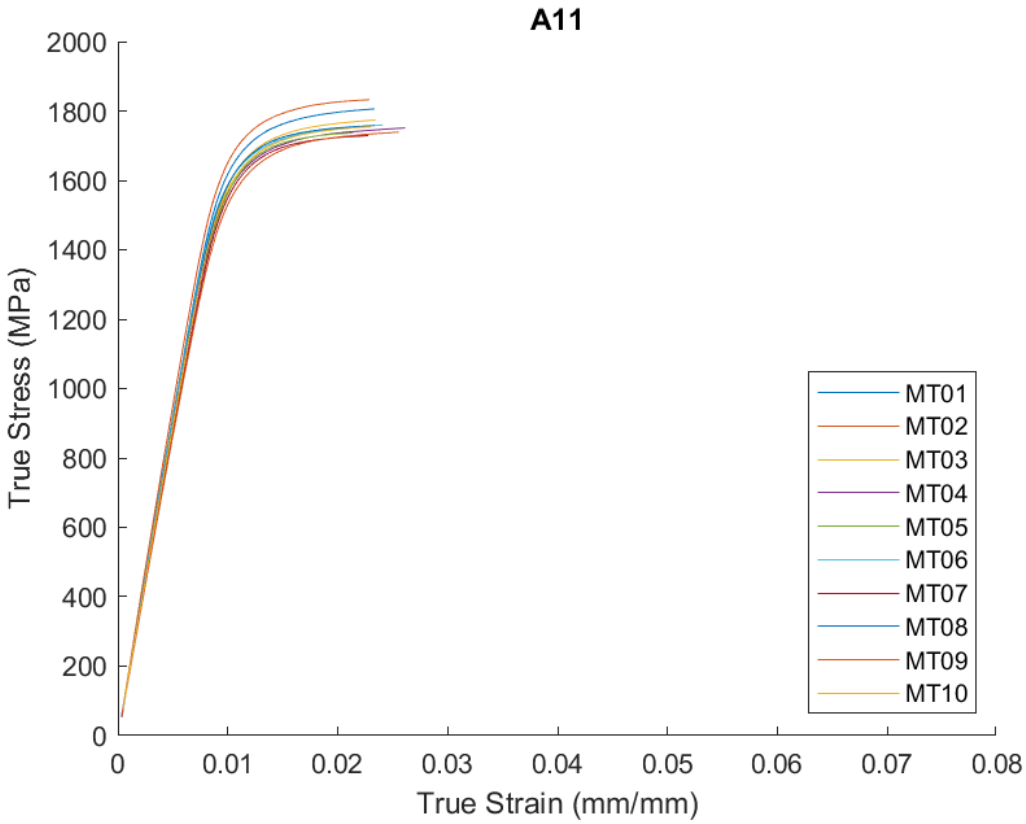

Fig. B10. True stress-strain curves for the A11 condition.

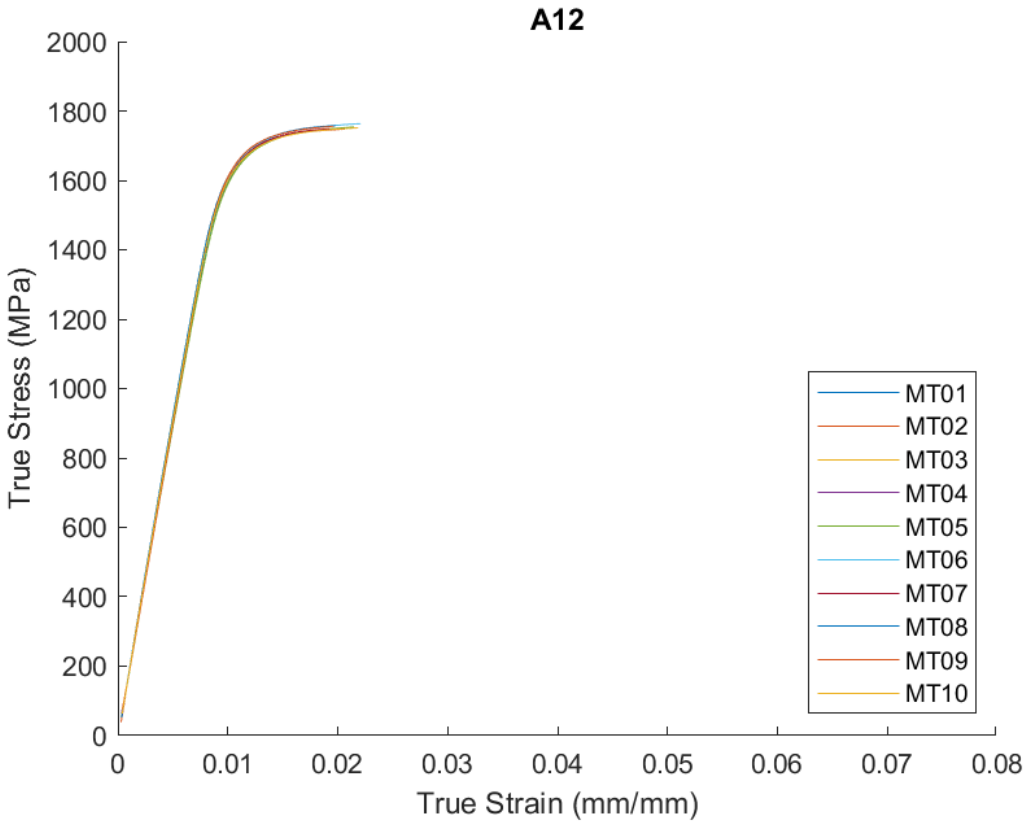

Fig. B11. True stress-strain curves for the A12 condition.

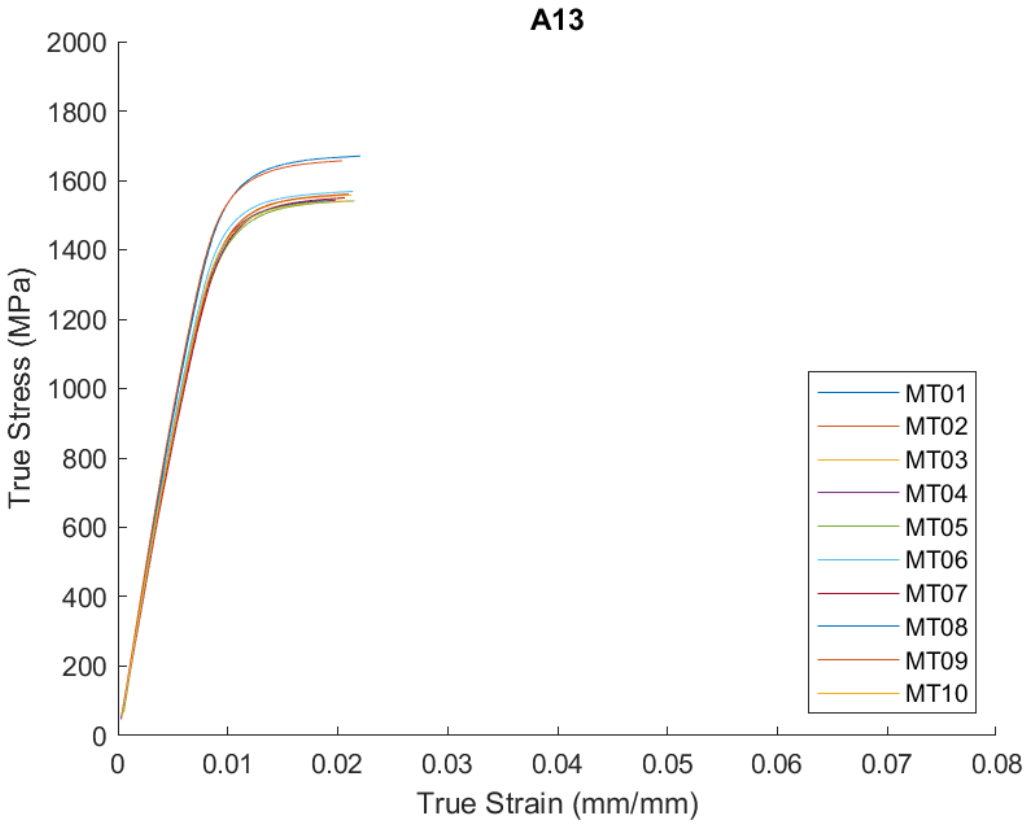

Fig. B12. True stress-strain curves for the A13 condition.

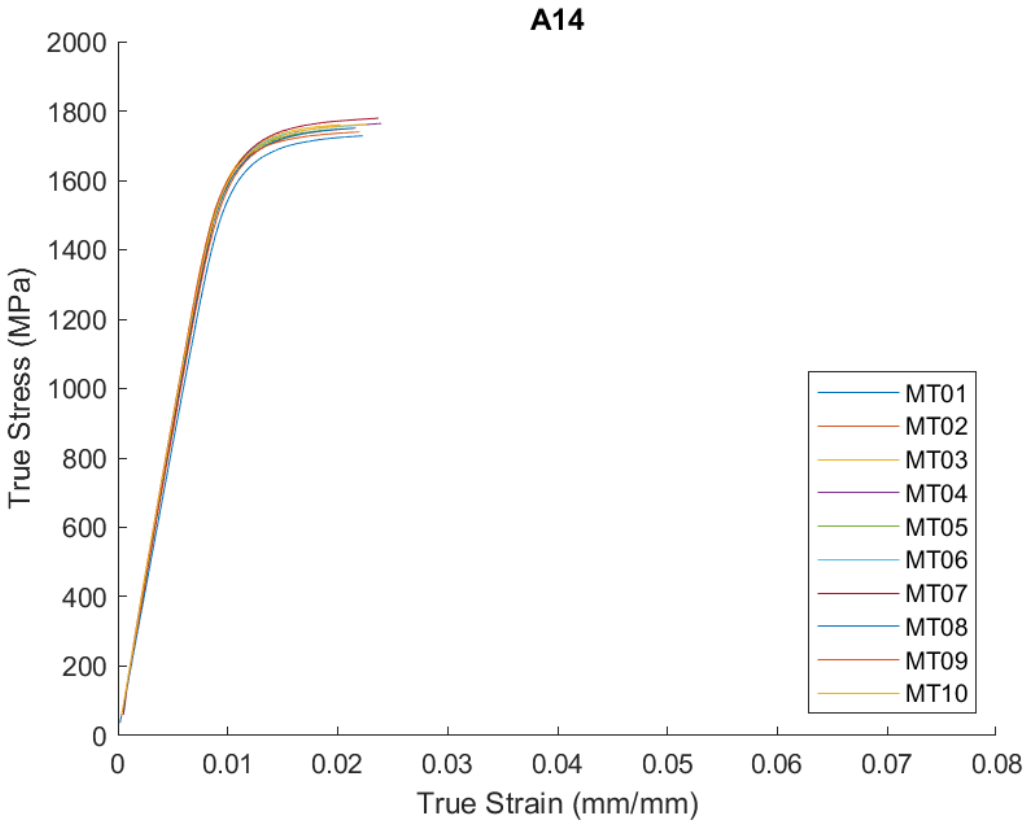

Fig. B13. True stress-strain curves for the A14 condition.

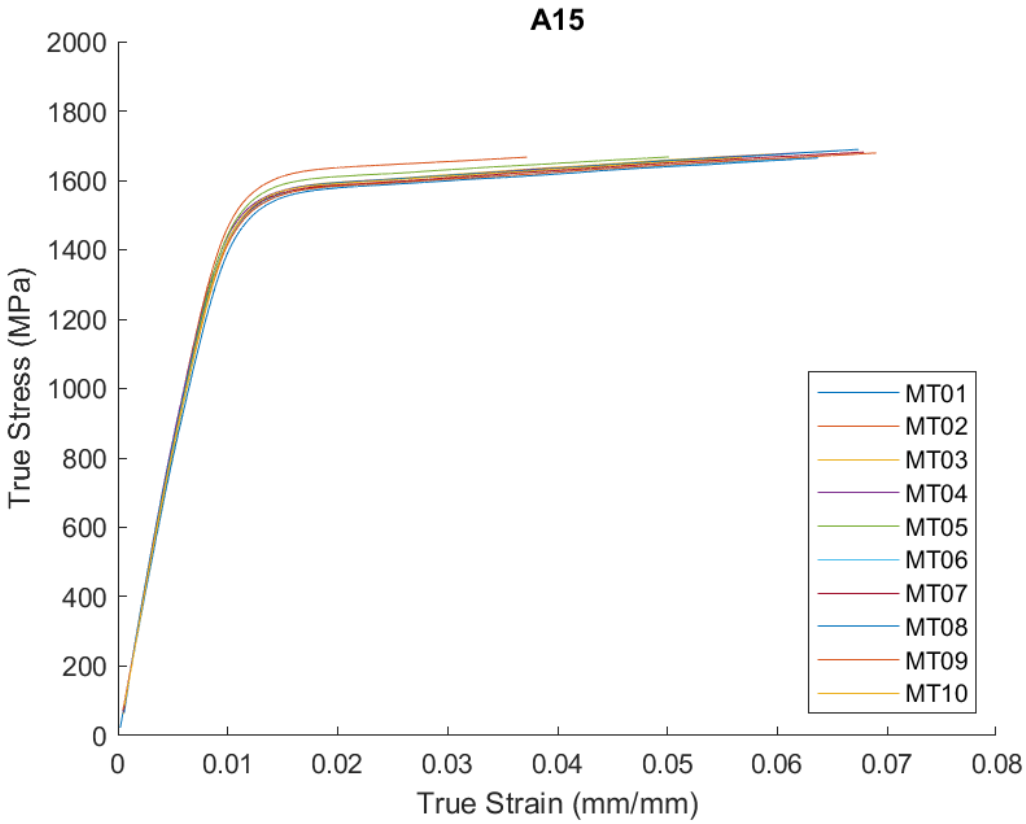

Fig. B14. True stress-strain curves for the A15 condition.

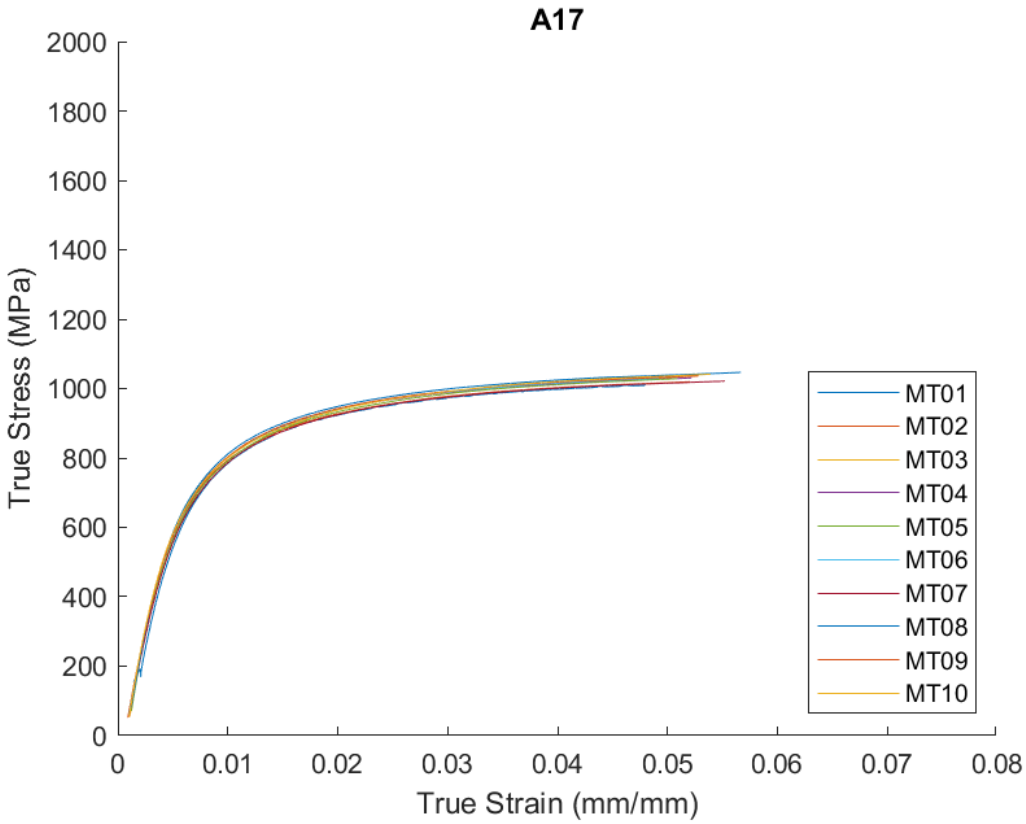

Fig. B15. True stress-strain curves for the A17 condition.

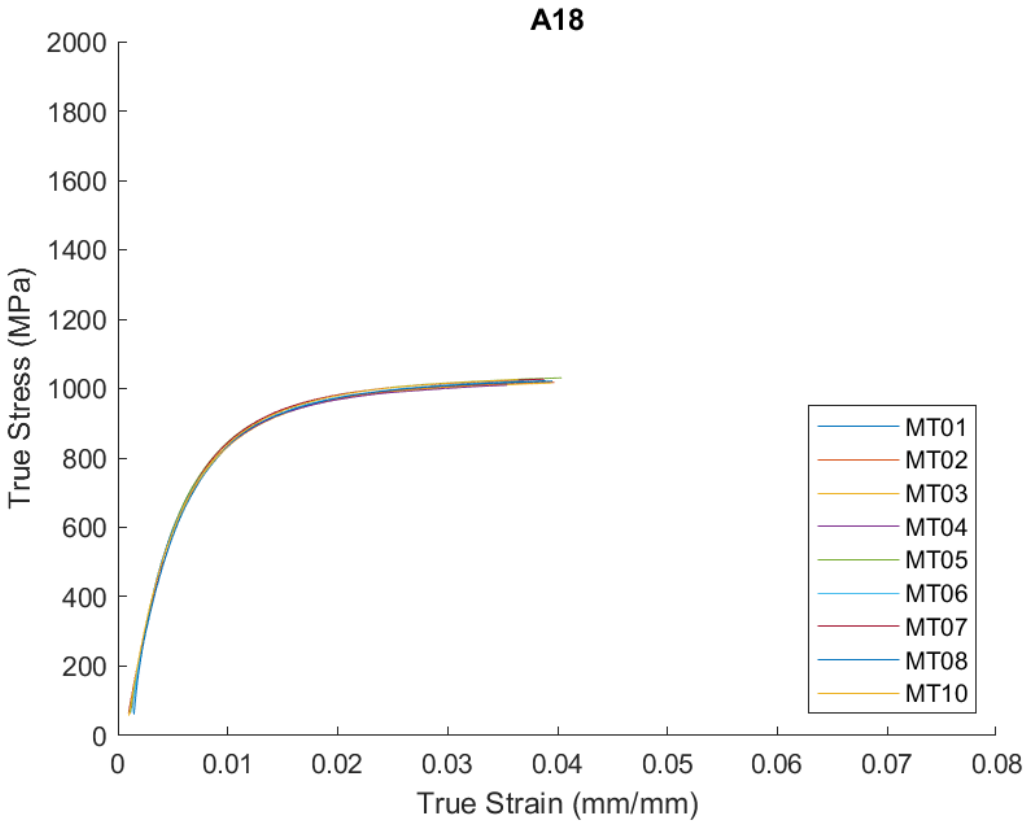

Fig. B16. True stress-strain curves for the A18 condition.

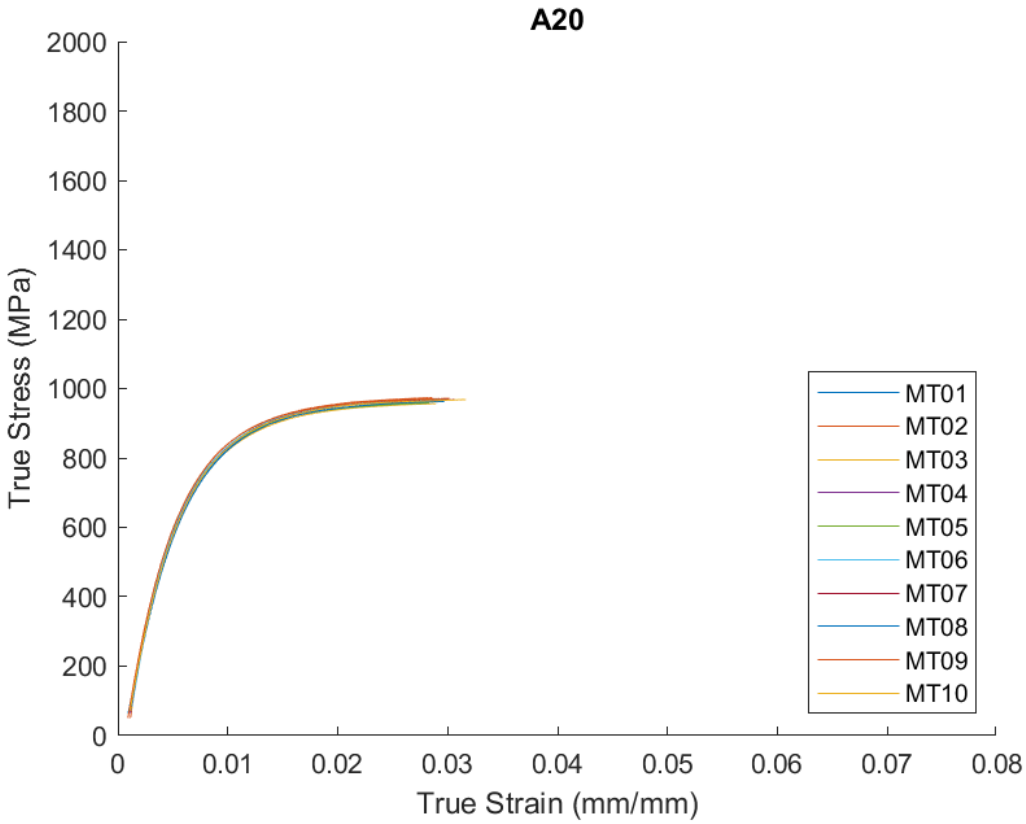

Fig. B17. True stress-strain curves for the A20 condition.

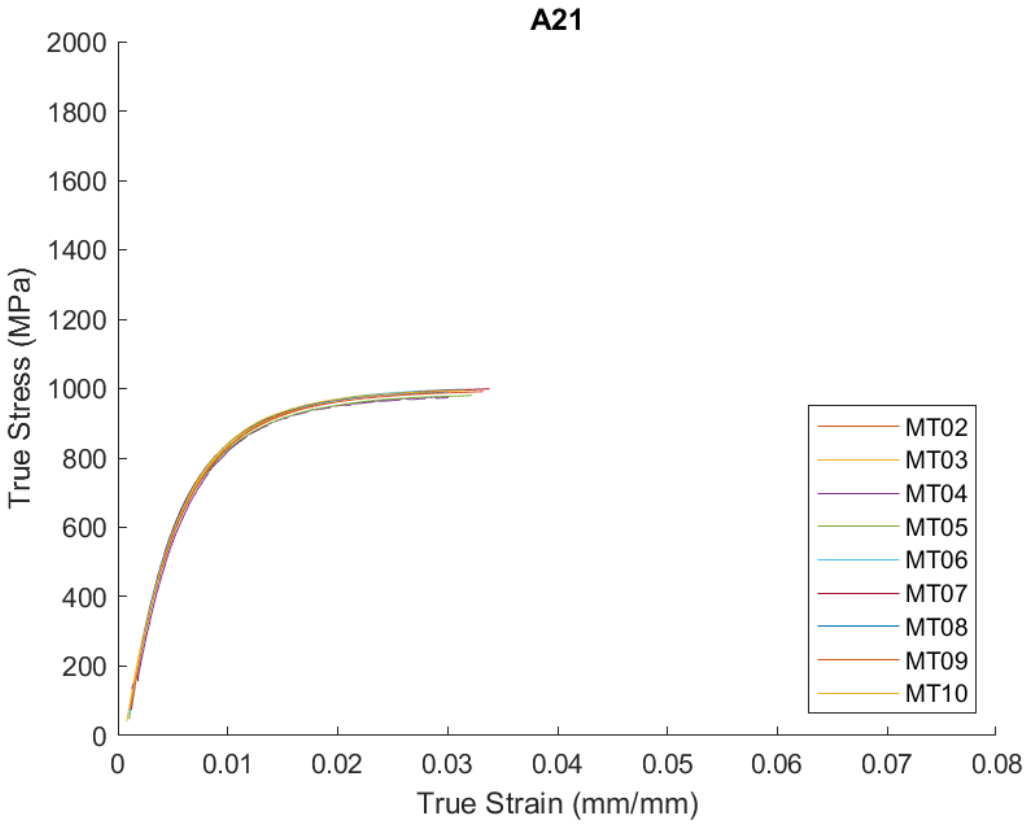

Fig. B18. True stress-strain curves for the A21 condition.

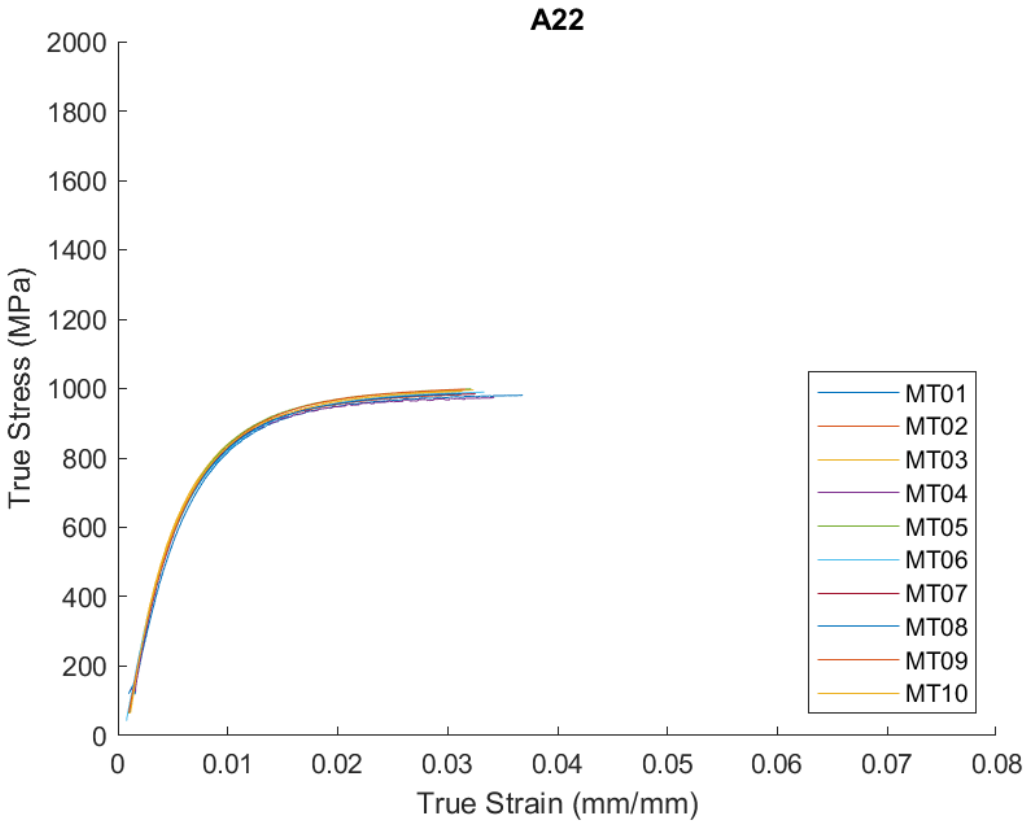

Fig. B19. True stress-strain curves for the A22 condition.

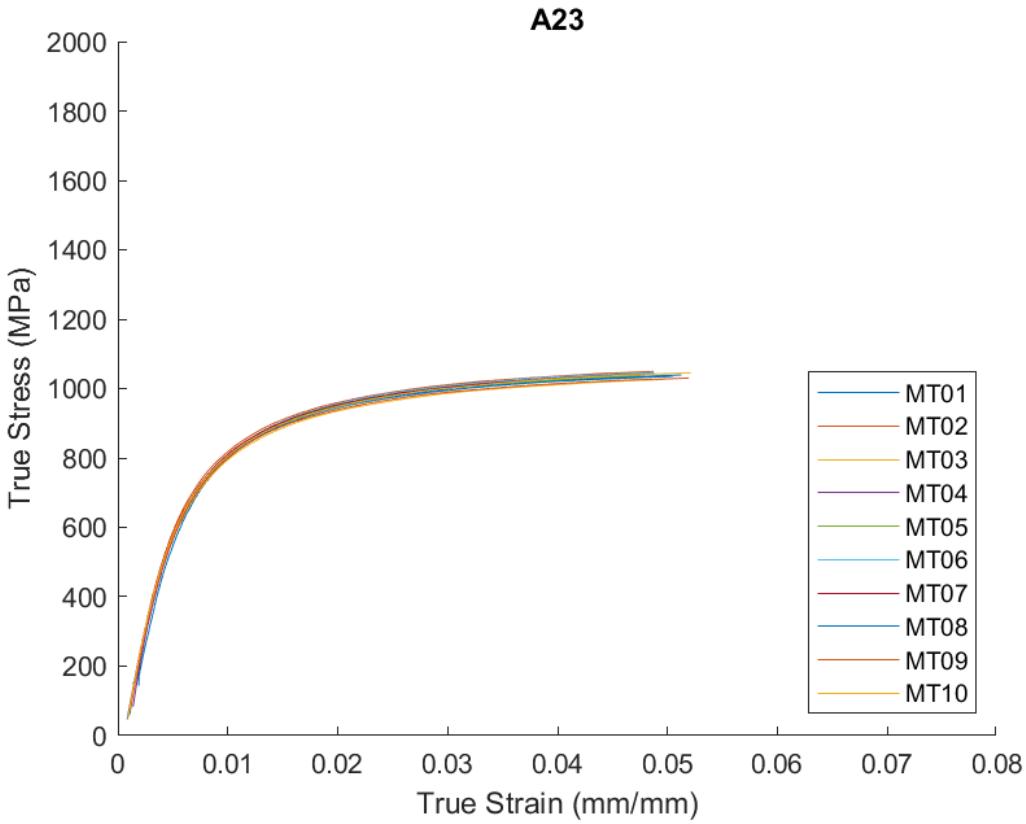

Fig. B20. True stress-strain curves for the A23 condition.

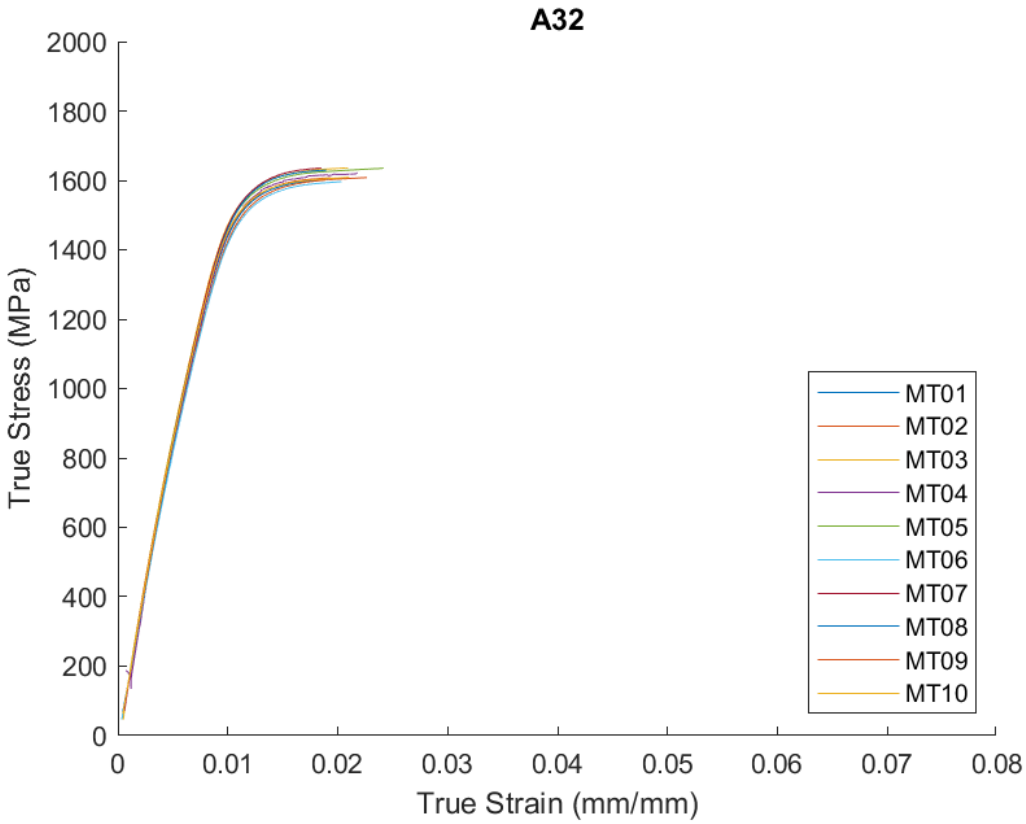

Fig. B21. True stress-strain curves for the A32 condition.

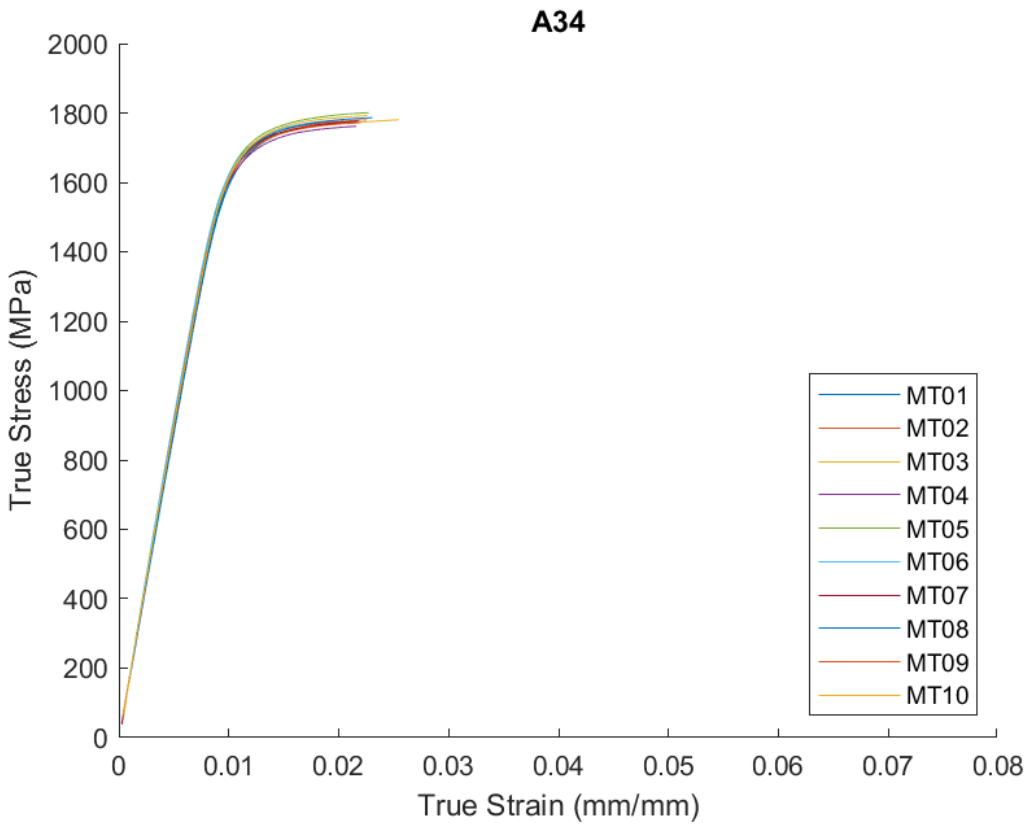

Fig. B22. True stress-strain curves for the A34 condition.

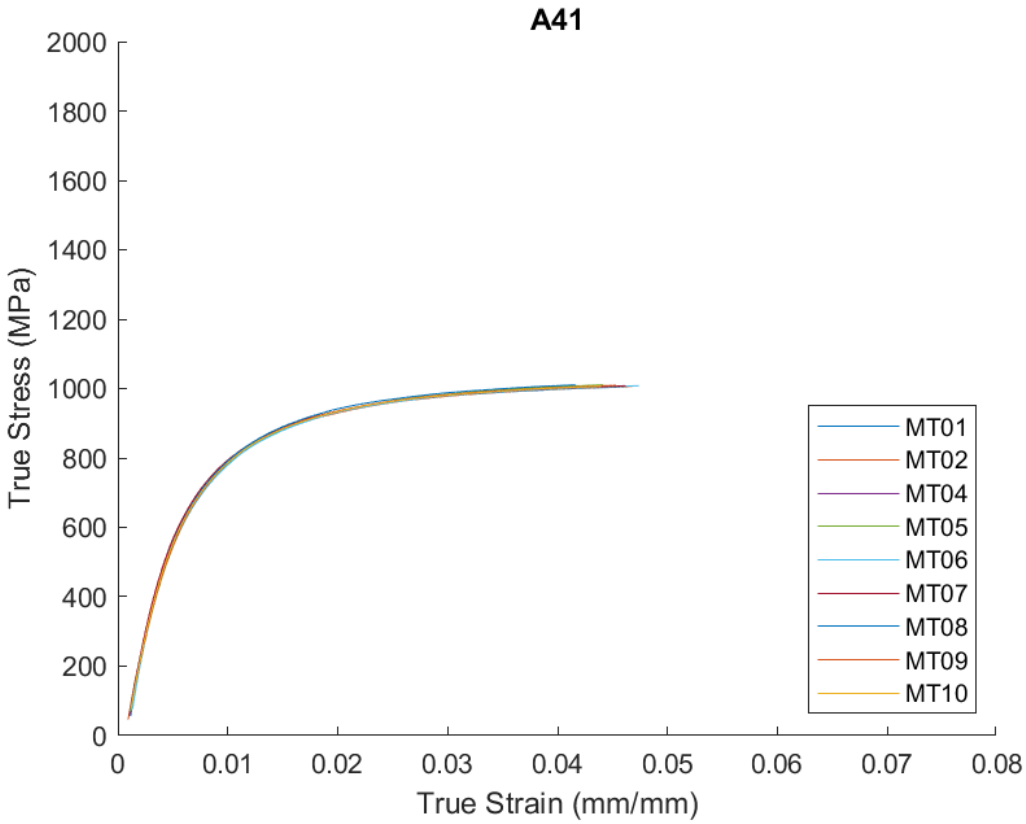

Fig. B23. True stress-strain curves for the A41 condition.

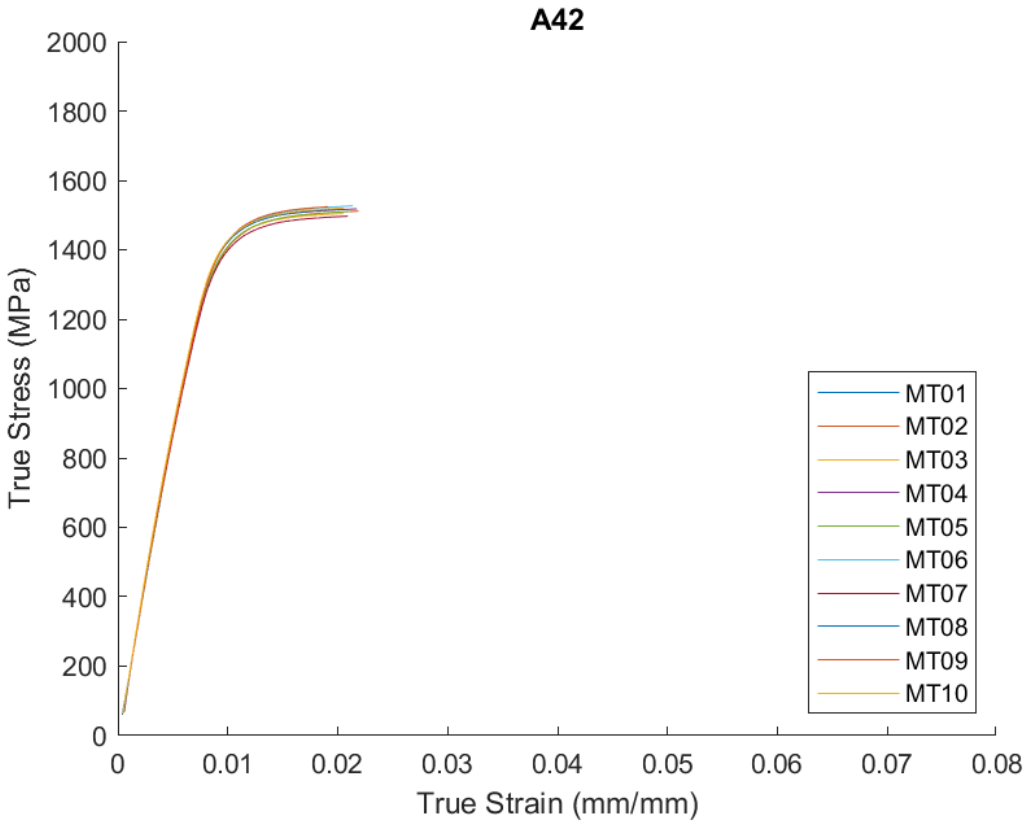

Fig. B24. True stress-strain curves for the A42 condition.